3-24-2019

Electron Biomolecule Collisions

Joshuah Anthony Trocchi
University of Windsor

Electron Biomolecule Collisions

By

Joshuah Anthony Trocchi

A Thesis
Submitted to the Faculty of Graduate Studies
through the Department of Physics
in Partial Fulfillment of the Requirements for
the Degree of Master of Science
at the University of Windsor

Windsor, Ontario, Canada

2019

Electron Biomolecule Collisions

by

Joshuah A. Trocchi

APPROVED BY:

R. Schurko

Department of Chemistry and Biochemistry

S. Rehse

Department of Physics

J.W. McConkey, Advisor

Department of Physics

January 31, 2019

Declaration of Co-authorship / Previous Publication

I. Co-Authorship.

I hereby declare that this thesis incorporates material that is result of joint research, as follows:

I acknowledge my supervisor, Dr. J.W. McConkey, for his contributions to the writing of this thesis, including edits and suggestions on the degree of discussion present in this work.

I also acknowledge J. Hein who designed the biomolecule oven used in this work and was a post-doctoral fellow under the supervision of Dr. J.W. McConkey. Also, some diagrams he made for use in the lab have been reproduced in this thesis with appropriate credit.

Chapter 4 contains work on thymine that is published. The data collection and analysis was initially conducted alongside C.J. Tiessen under the supervision of Dr. J.W. McConkey, which I concluded with follow-up analysis for this thesis. C.J. Tiessen also provided the vapour pressure fit of thymine using data from literature. Dr. W. Kedzierski and J. Dech assisted with data analysis and provided input on the operation of the experimental apparatus.

Chapter 5 contains work on adenine that is also published. I collected data and performed the data analysis under the supervision of Dr. J.W. McConkey while Dr. W. Kedzierski and J. Dech provided input on the operation of the apparatus. J. Dech also developed a program that would allow the computer in the lab to interface with the BNC565 pulse generator.

I am aware of the University of Windsor Senate Policy on Authorship and I certify that I have properly acknowledged the contribution of other researchers to my thesis, and have

obtained written permission from each of the co-author(s) to include the above material(s) in my thesis.

I certify that, with the above qualification, this thesis, and the research to which it refers, is the product of my own work.

II. Previous Publication.

This thesis includes 2 original papers that have been previously published/submitted for publication in peer reviewed journals, as follows:

Thesis Chapter	Publication title/full citation	Publication status
Chapter 4	C.J. Tiessen, J.A. Trocchi, J.D. Hein, J. Dech, W. Kedzierski, and J.W. McConkey. VUV Study of electron impact dissociative excitation of thymine. *Journal of Physics B: Atomic, Molecular and Optical Physics*, 49(12):125204, 2016.	published
Chapter 5	J.A. Trocchi, J. Dech, W. Kedzierski, J.W. McConkey. Production of excited H—atoms in Electron Collisions with Adenine. *Journal of Physics B: Atomic, Molecular and Optical Physics*, 10.1088/1361-6455/ab0222, 2019.	published

III. General.

I declare that, to the best of my knowledge, my thesis does not infringe upon anyones copyright nor violate any proprietary rights and that any ideas, techniques, quotations, or any other material from the work of other people included in my thesis, published or otherwise, are fully acknowledged in accordance with the standard referencing practices. Furthermore, to the extent that I have included copyrighted material that surpasses the bounds of fair dealing within the meaning of the Canada Copyright Act, I certify that I have obtained a written permission from the copyright owner(s) to include such material(s) in my thesis.

I declare that this is a true copy of my thesis, including any final revisions, as approved by my thesis committee and the Graduate Studies office, and that this thesis has not been submitted for a higher degree to any other University or Institution.

Abstract

A crossed electron-molecular beam system connected to a spectrometer was used to investigate the dissociative excitation of thymine and adenine following electron impact. The emission spectrum for these molecules was measured from 80 nm to 150 nm with a 100 eV electron beam to identify the excited atomic fragments that resulted from these electron collisions. For each molecule, the hydrogen Lyman series was dominant in spectrum measurements. Relative emission cross sections were measured with respect to Lyman-alpha for each the Lyman features present in the spectrum for each molecule. The probability of obtaining other atomic fragments from the parent molecules was concluded to be insignificant. Excitation studies were also performed to measure the relative emission cross sections for electron impact energies up to 430 eV. During thymine studies, this excitation study was performed for Lyman-alpha in which the threshold energy for this feature was measured to be 23 eV. During adenine studies, excitation studies were also performed for Lyman-alpha and Lyman-beta and their thresholds were determined to be 23 eV and 18 eV, respectively. The possible excitation and dissociation mechanisms from the parent molecules that may contribute to these studied features are also discussed.

For my parents, and for my sister.

Acknowledgements

First, I would like to thank Dr. J.W. McConkey, whose wisdom and patience could never be overstated. Additionally, I would like to thank Dr. Kedzierski for his advice and willingness to lend a helping hand. Both have been important mentors, and the lessons I have learned from them extend far from the field of physics.

Next, I would like to thank Collin Tiessen, who was a fellow student in the lab a few years back but made significant contributions to the experiment in general and helped me grow as a scientist. He has helped in many ways ever since he had left.

Additionally, gratitude is owed to Jeffrey Dech, who also worked in the lab and would never hesitate to spend time away from his own commitments and instead help me with a problem I was working on. He helped me become more confident in my work.

I would also like to thank Erik Clausen, Louis Beaudry, and Sinisa Jezdic, who all contributed to the development and maintenance of the experiment.

Finally, I would like to thank the rest of my friends, including Aaron Bondy, Daniel Venn, Spencer Percy, Maha Sami, Anmol Dahr, and many more for their support and encouragement.

Contents

List of Tables

List of Figures

Table of Abbreviations

Shortened Form	Phrase
VUV	Vacuum Ultraviolet
DNA	Deoxyribonucleic Acid
RNA	Ribonucleic Acid
SSB	Single Strand Break
DSB	Double Strand Break
DEA	Dissociative Electron Attachment
V-to-F	Voltage to Frequency
CEM	Channel Electron Multiplier
PMT	Photomultiplier
FWHM	Full Width at Half Maximum
TFA	Timing Filter Amplifier
CFD	Constant Fraction Discriminator
REMPI	Resonance-Enhanced Multiphoton Ionization

Chapter 1

Biomolecule Targets - Thymine and Adenine

1.1 Introduction

Collisions between an electron with an atom or molecule can not only change the momentum of the colliding objects but can also affect the electronic, vibrational, and rotational energy of the atom or molecule. Hence, electron collision experiments are performed to investigate dissociative, ionization, and excitation processes in a chosen target. If one is interested in such processes, one can measure the light that is emitted from targets or fragments (if the target undergoes dissociation) that have been promoted to an excited state; all that is needed is for the excited states to radiatively decay. This photon flux can be measured and related to the cross section of the excited state process that resulted from the collision.

If one has the capability to measure photon flux from an electron collision with their target across a range of wavelengths, then specific transitions and processes may be identified by measuring the spectral lines that occur. Additionally, once a feature has been identified, its energy dependence can be measured. This results in a so-called excitation function, a measure of photon flux (which can be related to the cross section of the exci-

tation process) against variation in energy. Measurement of the excitation function makes it possible to identify the energy threshold(s) responsible for the production of radiation of that wavelength.

In this work, a monoenergetic electron beam was used in tandem with a spectrometer and photon detector to study the excitation processes involved with some targets. Light of the vacuum ultraviolet (VUV) range of wavelengths (50 nm to 200 nm) was exclusively studied as many transitions belonging to atomic species (H, He, C, N, O, and more) are found in this spectral region.

The work done here is a continuation of prior work performed with the VUV spectrometer, where excitation processes were studied for some sulfur-containing molecules by Brotton et al. ([6] - [7]) and, more recently, a change in focus towards biomolecules with the pyrimidine work by Hein et al. [8]. Electron impact studies were performed on thymine and adenine in the VUV emission range.

1.2 Damage Mechanisms for DNA

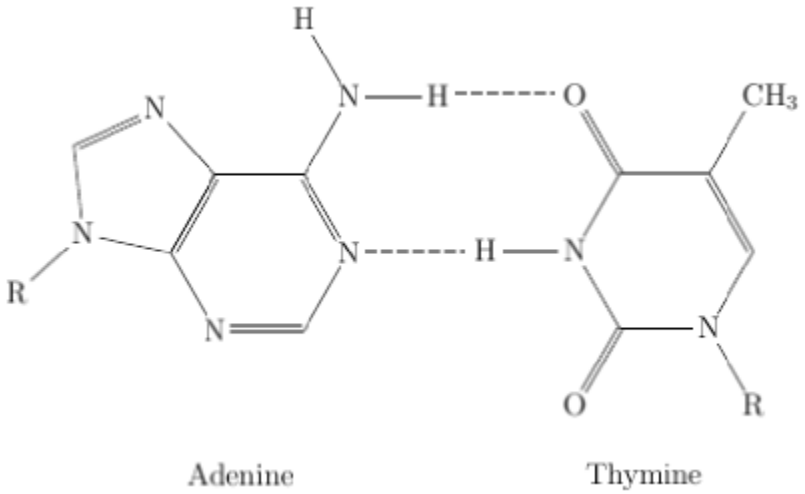

Figure 1.1: The adenine and thymine base pair hydrogen bonded together. The molecules connect to the phosphate-deoxyribose backbone at the R group as can be seen in the figure.

Thymine and adenine are two of the four nucleobases in the nucleic acids of DNA and

together form a complementary base pair (A-T) via two hydrogen bonds. The other two nucleobases, guanine and cytosine, form another base pair (G-C) via three hydrogen bonds. In RNA, thymine is substituted with uracil (demethylated thymine) and the base pairs are instead A-U and C-G. More generally, the nucleic acid in these nucleobases (DNA and RNA) consist of purines, which are the double ringed nitrogen-containing compounds, and their complementary pyrimidine partner, which are the single-ringed nitrogen-containing compounds. The importance of these nucleic acids can hardly be overstated. These molecules are responsible for encoding genetic information and are essential for all living cells [9].

The structure of DNA involves sequences of the aforementioned base pairs, which constitutes the genetic code. These base pairs are connected to a phosphate-deoxyribose backbone that is arranged in a double helix shape, which is useful for the DNA molecule as it allows DNA to readily replicate itself. This replication mechanism first involves breaking the hydrogen bonds between the complementary base pairs, which causes an "unzipping" of the double strand. Once the two strands are separated, an enzyme called DNA polymerase matches the isolated purine or pyrimidine with its complementary pair and bonds it to the strand. This mechanism allows a DNA molecule to copy itself — any one of the two strands can be used to preserve the genetic information, as the presence of a purine (adenine and guanine) or a pyrimidine (thymine and cytosine) suggests its complementary pair. T replication mechanism itself is very accurate, with less than one mistake in every 10^7 nucleotides copied [10].

However, DNA may be damaged by oxidising and alkylating agents, or by high energy radiation (like UV light or X-rays). Manifestations of this damage can include alteration of the A-T or G-C sequencing in the molecule, insertions or deletions of sequences, fragmentation of the backbone and as a result single strand or double strand breaks, cross-linking between the pyrimidine bases, and numerous other mechanisms. Most of this damage can be repaired, but not all of it, and the changes or errors in base pair sequencing can pass through the replication process uncorrected, which can lead to mutations that cause cancer.

Additionally, the general accumulation of these uncorrected errors may be an important cause of ageing [11].

Ionizing radiation (like X-rays or charged particles) can be absorbed by biological material, interact with critical nucleotide targets, and begin a process of events that leads to permanent change. The event whereby atoms or molecules of a nucleotide target are ionized or excited by incoming radiation is called direct action; for instance, an X-ray may be absorbed by the DNA molecule, which causes the production of secondary electrons, often 30 eV or lower [12], that can further interact with the biological environment. If instead ionizing radiation interacts with the surroundings, DNA may be damaged by the process of indirect action, whereby free radicals are produced and can interact with the DNA molecule. Both of these radiation damage mechanisms can readily cause single strand and double strand breaks. The first kind of inflicted damage is easily repaired, but the breaking of both strands is more serious. Double strand breaks can be repaired by an illegitimate recombination where the split ends are rejoined, but with no guiding template this process is prone to errors and may account for many premutagenic lesions induced in DNA [13].

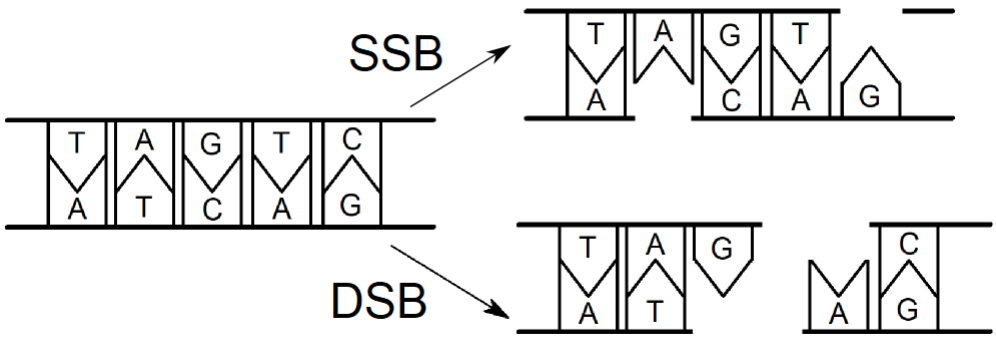

Figure 1.2: An illustration of single strand breaks (SSB) and double strand breaks (DSB) in DNA. Various A-T and G-C pairs are shown on the backbone. Single strand breaks are easily repaired, but double stand breaks are much more serious and can be the cause of mutations.

It is important to understand the dissociative, excitation, and ionization events that may occur in biological material as such information can be used to model radiation damage

processes, and so, much work has been done to fill in the gaps of information. Boudaiffa et al. [14] have shown that dissociative electron attachment (DEA) is a possible method causing single strand and double strand breaks. In work done by van der Burgt [15], a large body of work is referenced about the ionization of thymine, along with dissociative ionization, and also on DEA. In addition, a few review articles have been compiled, mainly Hotop et al.[16], Balog et al.[17], Sanche et al.[18], and Baccarelli et al.[19]. Colyer et al. [20] have performed elastic scattering from thymine at 100 eV and 500 eV, while Abouaf et al. [21] and Chernyshova et al. [22] have studied thymine's low energy electron-loss spectroscopy. Additionally, low energy elastic and inelastic scattering calculations on DNA bases have been performed by Winstead et al. [23] and Dora et al. [24].

There has been a wide volume of research performed to gather information on absolute cross sections for various kinds of collisions with the DNA bases along with identifying fragmentation pathways and dissociation events in order to steadily build up a bank of information that can be used to help develop theoretical models more accurately estimate biological damage from collisional processes. However, a limited number of studies are available that involve photon emission following electron impact. Work has been performed in the visible and near UV spectral regions to investigate radiation from molecular fragments, including uracil, by Shafranyosh et al. in reference [25] and reference [26] and Shpenik et al. in reference [27] and reference [28]. Despite numerous studies, there is a lack of work done to identify excited atomic species following electron impact. The work presented in this thesis is an attempt to remedy this gap of information and to continue similar studies that were performed with pyrimidine in this lab [8]. In this work, photo emission following electron impact on thymine and adenine was measured for wavelengths of light between 80 nm and 140 nm. As the primary emissions in this range are due to excited atomic states, the work for this thesis involve identifying the primary atomic fragments resulting from electron collisions and making measurements on the cross sections for the features present. Absolute cross sections could not be measured in this work as the vapour pressure of the molecular

beams could not be measured, but other data can be obtained. Following the identification of atomic fragments resulting from electron bombardment by measuring an emission spectrum over the 80 nm to 140 nm wavelength range, the emission cross sections for features present in the spectral range could be measured relative to the largest feature found. In this way, if the absolute cross section for any one of these emission features were measured, as may be done in future work, then the relative emission cross section work present here may be used to determine absolute cross section measurements for the other features.

Once a spectral feature was identified, excitation studies were performed on the feature to measure the cross section's dependence on electron impact energy. Specifically, these excitation studies yield measurements of the electron impact energy where the cross section is at a maximum and also provides some insight into the high energy behaviour of the cross sections. Additionally, the threshold energy for atomic dissociations from the parent molecules can be measured, and as the electron impact energy rises, additional thresholds representative of newly dominant dissociation pathways that yield the atomic spectral feature under observation can also be identified as they become relevant to the total cross section. These threshold observations are discussed in the context of literature where mass spectrometry and photofragmentation measurements have been performed for thymine and adenine.

Mass spectrometry work done by Rice et al. [29] measured mass fragments of thymine and adenine, while other thymine mass spectra were obtained by Ulrich et al. [30]. and Imhoff et al. [31]. Prominent mass fragments had been clearly identified in these works and fragmentation of the parent molecules was achieved with electron impact energies comparable to the energies used in this work. Sethi et al. [32] performed mass spectrometry for adenine with electron ionization spectra. In the work of Minaev et al. [2], absolute total ionization cross sections up to 200 eV for adenine have been measured. Jochims et al. [33], Schneider et al. [34], and Li et al. [35] have performed photon impact studies on isolated nucleobases. Particularly in the work of Jochims, 6 to 22 eV synchrotron radiation was used to probe the photofragmentation of adenine, thymine, and uracil where fragmentation

pathways are discussed. van der Burgt et al. [12] have measured partial ionization cross sections for positive fragments of adenine following electron impact. Dawley et al. [36] have measured electron ionization of adenine and Pilling et al. [37] have measured the dissociative photoionization of adenine. The results from the works discussed here are compared later to the results obtained for excitation studies of the identified emission atomic spectral features. This is done to check for possible fragmentation mechanisms that may be responsible in producing the studied feature and therefore determine the importance of such fragmentation pathways to the total cross section of the studied feature.

Chapter 2

Electron Collisions

2.1 Elastic and Inelastic Collisions

When one considers the action of an electron colliding into some target, numerous kinds of scattering processes are possible. An electron can collide with a target and scatter without losing any energy but change the individual momenta of the involved species in a process called elastic scattering. An atom, A, as an example, will not have its internal energy changed.

$$e + A \rightarrow e + A \tag{2.1}$$

Electrons with sufficient energy may also affect the internal structure of its target. If a collision process occurs between an electron and a target, the electron may transfer some energy to the target and affect its internal structure - this is called inelastic scattering. For instance, the example atom A that was considered above, if hit by an electron e, which can become captured:

$$e + A \rightarrow A^{-} \tag{2.2}$$

In another case, an electron can inelastically collide into the target A and transfer some

of its energy to the target.

$$e + A \rightarrow e' + A^* \tag{2.3}$$

e' denotes the scattered electron while A^* denotes the excited state of the atom, which some timer later can optically decay to its ground state. Another inelastic scattering process is the action of ionization, where the projectile electron strips the target of one its own electrons, denoted by e'' in the equation below.

$$e + A \rightarrow e' + e'' + A^+ \tag{2.4}$$

In this case, the collision has produced an ion. An electron impact that results in multiple ionizations is possible, but usually with higher kinetic energy of the projectile electron, or with heavier atoms that possess more electrons. Additionally, ionization of the target can occur alongside an excitation process.

Similar processes can also be described for molecules. If we consider a diatomic molecule made up of atom A and atom B, the different scattering channels as described before are easily accounted for.

$$e + AB \rightarrow AB^- \tag{2.5}$$

$$e + AB \rightarrow e + AB \tag{2.6}$$

$$e + AB \rightarrow e' + AB^* \tag{2.7}$$

$$e + AB \rightarrow e' + e'' + AB^+ \tag{2.8}$$

In addition to these kinds of collisions, an electron with sufficient kinetic energy can

easily break any bonds that constitute the molecule.

$$e + AB \rightarrow e' + A + B \tag{2.9}$$

This is a simple dissociation of the diatomic molecule AB. It is feasible for dissociative processes to occur concurrently with absorption by one of the fragments, or with the promotion of a fragment to an excited state whereby it itself can radiatively decay, or with ionization. Due to the increase in internal complexity of molecules, many more scattering channels are opened up for them compared to atoms.

In this work, we are primarily concerned with collision events that result in the production of excited products, more specifically, excited atomic fragments following electron impact on biomolecules.

2.2 Quantum Treatment of Scattering

The following discussion is a basic theoretical introduction to the differential cross section for non-relativistic collisions, which will facilitate discussion on the Bethe-Born approximation, which itself is discussed in the subsequent section. The physical consequences of the Bethe-Born approximation are used in the analysis of the relative cross section measurements obtained during excitation studies for energies beyond the cross section maxima. The discussion here follows the treatment by Inokuti [38]. By the end of this section, we will arrive at an equation for the total cross section, and then move on to discuss the Bethe-Born approximation for high energies.

First consider an excitation collision process between an electron and a ground state target (atom) with Z electrons where the atom transitions from a ground state to an excited state n. At non-relativistic but high kinetic energies, we may determine the differential cross section $d\sigma_n$ using the first Born approximation for scattering. First by identifying $\vec{p_0}$ as the momentum of the electron before the collision, $\vec{p}$ as the momentum of the electron after the

collision, and the momentum transfer as $\vec{K} = \vec{p} - \vec{p_0}$, the differential cross section $d\sigma_n$ for a solid angle $d\omega$ at θ and ϕ, calculated in the lowest order of the interaction potential V between the electron and target is given by the following equation in atomic units.

$$d\sigma_n = \frac{m^2 p}{4\pi^2 p_0} \left(\int e^{i\vec{K}\cdot\vec{r}} u_n^*(\vec{r_1}...\vec{r_z}) V u_0(\vec{r_1}...\vec{r_z}) d\vec{r_1}...\vec{r_z}d\vec{r}) \right)^2 d\omega \tag{2.10}$$

The quantity m is simply the reduced mass of the two-body system, given as:

$$m = \frac{m_1 m_2}{m_1 + m_2} \tag{2.11}$$

In the integrand, u_0 and u_n are the bound state wave functions of the target at the ground state and the nth state, respectively. The quantity $\vec{r}$ is the position of the projectile electron while any $\vec{r_i}$ is the position of the ith electron in the target.

Next, we consider a Coulombic interaction between the projectile and its target.

$$V = \sum_{j=1}^{Z} \frac{e^2}{\mid \vec{r} - \vec{r_j} \mid} - \frac{Ze^2}{r} \tag{2.12}$$

From here, we follow the work by Bethe [39], where we introduce the following relation.

$$\int \frac{e^{i\vec{K}\cdot\vec{r}}}{\mid \vec{r} - \vec{r_j} \mid} d\vec{r} = \frac{4\pi}{K^2} e^{i\vec{K}\cdot\vec{r_j}} \tag{2.13}$$

This expression allows us to modify Equation 2.10.

$$d\sigma_n = \frac{4m^2 e^4 p}{K^4 p_0} \mid \epsilon_n(K) \mid^2 d\omega \tag{2.14}$$

$\epsilon_n(K)$ is the atomic matrix element of the target. It is written as

$$\epsilon_n(K) = \langle n | \sum_{j=1}^{Z} e^{i\vec{K}\cdot\vec{r_j}} | 0 \rangle \tag{2.15}$$

or alternatively:

$$\epsilon_n(K) = \int u_n^* \sum_{j=1}^{Z} e^{i\vec{K}\cdot\vec{r_j}} u_0 d\vec{r_1}...d\vec{r_Z} \tag{2.16}$$

We now consider two more items of interest. Firstly, we seek to replace $d\omega$ by $2\pi sin\theta d\theta = \pi d(K^2)/pp_0$. Secondly, as the states $|n\rangle$ and $|0\rangle$ are orthogonal, the second term in Equation 2.12 for the interaction potential, vanishes. We arrive at the following equation.

$$d\sigma_n = \frac{4\pi m^2 e^4}{p_0^2 K^4} \mid \epsilon_n(K) \mid^2 d(K^2) = \frac{4\pi m^2 e^4}{p_0^2 K^2} \mid \epsilon_n(K) \mid^2 d\ln(Ka_0)^2 \tag{2.17}$$

where we have made use of the Bohr radius a_0 in Equation 2.17.

Next we define what is known as the Generalized Oscillator Strength, $f_n(K)$ in the next equation.

$$f_n(K) = \frac{E_{n0}}{R(Ka_0)^2} \mid \epsilon(K) \mid^2 \tag{2.18}$$

The term E_{n0} is the excitation energy of a target from its ground state to its nth state. The quantity R is the Rydberg energy. We will use this $f_n(K)$ as defined above in the latest expression for $d\sigma_n$.

$$d\sigma_n = \frac{4\pi e^4 m^2 a_0^2 R}{p_0^2 E_{n0}} f_n(K) d\ln(Ka_0^2) \tag{2.19}$$

During an electron collision with a target of mass M, we can assume the target is stationary as $M > m_e$. The relative momentum, p_0, can be written as $p_0 = mv$. Using the kinetic energy K_E of the projectile electron, the above equation becomes:

$$d\sigma_n = \frac{4\pi R^2 a_0^2}{K_E E_{n0}} f_n(K) d\ln(Ka_0)^2 \tag{2.20}$$

If we integrate across all possible values of $\ln(Ka_0)^2$, we can obtain the total cross section. If we define the following expressions,

$$\delta_0 = \ln(Ka_0)^2_{min} \tag{2.21}$$

and

$$\delta_1 = \ln(Ka_0)^2_{max} \tag{2.22}$$

then we can write the effective excitation cross section from the ground state to the nth excited state as in Equation 2.23.

$$\sigma_n = \frac{4\pi a_0^2 R^2}{K_E E_{n0}} \int_{\delta_0}^{\delta_1} f_n(K) d\ln(Ka_0)^2 \tag{2.23}$$

This completes our initial objective. Next we will examine the consequences of the asymptotic behaviour of $f_n(K)$ as $K \to 0$, and looking at an integration across all $\ln {Ka_0}^2$, i.e., letting the δ_0 and δ_1 defined earlier go to $-\infty$ and $+\infty$, respectively.

2.3 The Bethe-Born Approximation

Bethe [39] worked out a method for expressing the cross section as determined in Equation 2.23 in terms of an asymptotic expansion in inverse powers of K_E, which works very well at high energies. Given this, we now consider the integral limits, δ_0 and δ_1, and the behaviour of $f_n(K)$.

Looking at the asymptotic behaviour of the Generalized Oscillator Strength as K goes to 0, we get the optical oscillator strength, f_n.

$$\lim_{K \to 0} f_n(K) \tag{2.24}$$

For optically forbidden processes, the optical oscillator strength vanishes, i.e. $f_n = 0$. Then, as K approaches its lower limit, as defined by $(Ka_0)^2 \to 1/K_E$, $f_n(K)$ goes to 0. In the high energy approximation, $\delta_0 = \ln(Ka_0)^2_{min} \to -\infty$ and $\delta_1 = \ln(Ka_0)^2_{max} \to +\infty$. Then, we can arrive at expressions for the excitation cross sections of optically allowed processes

(Equation 2.25) and optically forbidden processes (Equation 2.26):

$$\sigma_n = \frac{4\pi a_0^2 R}{K_E}\left(M_n^2 \ln\left(\frac{4C_n T}{R}\right) + \frac{\gamma_n R}{K_E} + O\left[\left(\frac{E_{n0}}{K_E}\right)^2\right]\right) \tag{2.25}$$

$$\sigma_n = \frac{4\pi a_0^2 R}{K_E}\left(b_n + \frac{\gamma_n R}{K_E} + O\left[\left(\frac{E_{n0}}{K_E}\right)^2\right]\right) \tag{2.26}$$

M_n^2 is the dipole matrix element, as in:

$$M_n^2 = \frac{f_n R}{E_{n0}} \tag{2.27}$$

The other two terms, γ_n and b_n, are expressed in the following equations.

$$\gamma_n = -\frac{m_e f_n}{2m} - \left(\frac{E_{n0}}{4R}\right)\left[\frac{df_n(K)}{d(Ka_0^2)}\right]_{K=0} \tag{2.28}$$

$$b_n = \int_{-\infty}^{+\infty} \frac{R f_n(K)}{E_{n0}} d\ln(Ka_0)^2 \tag{2.29}$$

At the high energy limit where $K_E \to \infty$, the equations obtained for the optically allowed processes become:

$$\sigma_n = \frac{4\pi a_0^2 R M_n^2 \ln K_E}{K_E} + \frac{C}{K_E} \tag{2.30}$$

with C defined as:

$$C = 4\pi a_0^2 R M_n^2 \ln\left(\frac{4C_n}{R}\right) \tag{2.31}$$

Additionally, the optically forbidden process becomes:

$$\sigma_n = \frac{4\pi a_0^2 R b_n}{K_E} \tag{2.32}$$

Consider the cross section for an optically allowed process, as in Equation 2.30. One may plot $\ln K_E$ on a horizontal axis and $K_E\sigma_n$ on a vertical axis; doing so, with this process,

will yield a straight line with a slope proportional to M_n^2, and therefore the optical oscillator strength f_n. Additionally, the intercept on the horizontal axis yields C in Equation 2.30, and hence C_n. This technique was developed by Fano [40], and this plot itself is called a Fano plot. At high kinetic energies, a Fano plot indicating linear behaviour justifies the use of Bethe theory for the collision process. Absolute cross section data then makes it possible to obtain optical oscillator strengths. Note that if a Fano plot is made of an optically forbidden process, as in Equation 2.32, a linear function will not be made. Instead, this technique will yield a constant for the plot.

In this work, the Fano plot technique was used with measurements made on the total cross section for an excited atomic state, which provides a quantitative method for concluding whether the process is an optically allowed transition or optically forbidden but spin allowed transition. In the case of a high energy cross section for a spin forbidden transition, the cross section will decrease as $1/E^3$; this was not observed in this work. The experimental apparatus only had the capability to measure the cross section up to 430 eV; to properly test the Bethe-Born approximation on the cross section would require at least 1 keV, but the energy limit in this experiment does suffice to examine some differences between the optically allowed and optically forbidden but spin allowed transitions.

2.4 Photon Spectroscopy

We next consider a multichannel scattering event such as in a crossed-beam experiment, specifically with electrons and and molecules. The pressure of the gas that is used in the crossed-beam experiment, along with the electron beam current, should be sufficiently low so that some other secondary processes, like intrapopulation collisions and resonance absorption, negligibly contribute to the overall process. In a crossed-beam experiment, we consider a quantity $n(j)$, which is the number density of the jth excited target in the collision region.

It is given by the following equation.

$$\frac{dn(j)}{dt} = -\sum_{k;\, k<j} n(j)A(jk) + \frac{n(g)Q(j)IL}{e} + \sum_{i;\, i>j} A(ij)n(j) \tag{2.33}$$

$A(jk)$ and $A(ij)$ are the Einstein A coefficients for the transition to the kth/jth state from the jth/ith state, respectively. The number densities for the ground, ith state, and jth excited state atoms are $n(g)$, $n(i)$, and $n(j)$, respectively. $Q(j)$ is the excitation cross section for the transition to the jth state from the ground state. I is the electron current and L is the interaction length for the electron-target collision.

The equation listed above has three key terms. The first term describes the rate where the target of the jth excited state radiatively decays to the lower kth state while the third term describes the cascade contributions from higher states. The second term, in the middle, describes the electron impact excitation of atoms to the jth excited state from the ground state.

Consider when equilibrium is reached. This means that $dn(j)/dt = 0$ and $n(j)$ can be expressed using the terms in Equation 2.33.

$$n(j) = \frac{\left[\frac{n(g)Q(j)IL}{e} + \sum_{i;\, i>j} A(ij)n(i)\right]}{\sum_{k;\, k<j} A(jk)} \tag{2.34}$$

Next, we define the quantity $J(jk)$

$$J(jk) = \frac{n(j)A(jk)}{L} \tag{2.35}$$

which is the rate of targets in the jth state that decay to the kth state per unit length of the electron beam. $J(jk)$ can be substituted into the equation we just developed for $n(j)$.

$$J(jk) = \frac{\left[\frac{n(g)Q(j)I}{e} + \sum_{i;\, i>j} J(ij)\right] A(jk)}{\sum_{k';\, k'<j} A(jk')} \tag{2.36}$$

We would like to rearrange Equation 2.36 so that we can arrive at an expression for $Q(j)$, but first we can make use of the branching ratio for the jth to kth transition, $B(jk)$, to simplify the expression above. The branching ratio is defined as follows.

$$B(jk) = \frac{A(jk)}{\sum_{k';\, k'<j} A(jk')} \tag{2.37}$$

With this in hand, we are set to rearrange for $Q(j)$.

$$Q(j) = \frac{\left[\frac{J(jk)}{B(jk)} - \sum_{i;\, i>j} J(ij)\right] e}{n(g)I} \tag{2.38}$$

This equation reduces simply if the cascade contributions, $\sum_{i;\, i>j} J(ij)$, are negligible. $Q(j)$ can now be expressed as:

$$Q(j) = \frac{J(jk)e}{B(jk)n(g)I} \tag{2.39}$$

Using the relation,

$$B(jk) = \frac{J(jk)}{\sum_{k';\, k'<j} J(jk')} \tag{2.40}$$

Equation 2.39 can also be expressed in this way.

$$Q(j) = \frac{\sum_{k';\, k'<j} J(jk')e}{n(g)I} \tag{2.41}$$

This equation suggests that the excitation cross section for a transition to the jth state can be determined by measuring the radiation that is emitted from any transitions that end at the jth state. Spectral line intensities, $J(jk)$ are measured during photon spectroscopy experiments. A measurement of this kind readily provides a way to determine the effective cross section, $Q(jk)$, as long as $n(g)$ and I are measured too.

$$Q(jk) = \frac{J(jk)e}{n(g)I} \tag{2.42}$$

We next consider the problem of polarized radiation briefly. The polarization, P, is

defined as

$$P = \frac{\mathcal{I}_{\parallel} - \mathcal{I}_{\perp}}{\mathcal{I}_{\parallel} + \mathcal{I}_{\perp}} \tag{2.43}$$

In the above equation, the photon fluxes, $\mathcal{I}_{\perp}$ and $\mathcal{I}_{\parallel}$, emitted from the interaction region per unit solid angle in a direction that is orthogonal to the beam axis are related to the j→k transition resulting from the inelastic electron collisions. Specifically, they are the components of the electric dipole transition moment operator, for this j→k transition, for every atom or molecule in the interaction region. $\mathcal{I}_{\perp}$ is perpendicular to the electron beam axis while $\mathcal{I}_{\parallel}$ is parallel to the electron beam axis.

Following work done by Heddle and Keesing [41], the flux of photons that enter into unit solid angle in the direction of polar angle θ for a $j \rightarrow k$ transition can be written as:

$$J(jk,\theta) = \mathcal{I}_{\parallel}(jk)sin^2\theta + \mathcal{I}_{\perp}(jk)cos^2\theta + \mathcal{I}_{\perp}(jk) = [\mathcal{I}_{\parallel}(jk) + \mathcal{I}_{\perp}(jk)](1 - Pcos\theta) \tag{2.44}$$

We can obtain $J(j,k)$ by integrating over all angles, θ and ϕ; this integration results in the total intensity for the $j \rightarrow k$ transition.

$$J(jk) = \int_{4\pi} J(jk,\theta)d\omega \tag{2.45}$$

$$J(jk) = \frac{8\pi}{3}[\mathcal{I}_{\parallel}(jk) + 2\mathcal{I}_{\perp}(jk)] \tag{2.46}$$

This result can be used in Equation 2.42 to obtain an expression for $Q(jk)$ in a different form, utilizing the parallel and perpendicular photon intensities. Measurement of these intensities can yield a measurement of the effective cross section.

$$Q(jk) = \frac{8\pi}{3}\frac{\mathcal{I}_{\parallel}(jk) + 2\mathcal{I}_{\perp}(jk)}{n(g)I} \tag{2.47}$$

Next, we consider the differential cross section, defined as

$$q(jk,\theta) = \frac{J(jk,\theta)e}{n(g)I} \tag{2.48}$$

This can be simplified by defining an $a(jk)$ with the total intensity term, $\mathcal{I}_{\parallel} + \mathcal{I}_{\perp}$, as

$$a(jk) = \frac{(\mathcal{I}_{\parallel} + \mathcal{I}_{\perp})e}{n(g)I} \tag{2.49}$$

Then, in conjunction with the far right term in Equation 2.44, the differential cross section can be rewritten as

$$q(jk,\theta) = a(jk)(1 - Pcos^2\theta) \tag{2.50}$$

Note that $a(jk) = q(jk, 90°)$, the differential cross section at 90°, as from Equation 2.44, $Pcos(90°) = 0$, and $J(jk,\theta)$ is simply the sum of the intensities.

Integrating the differential cross section over a 4π solid angle yields the effective cross section:

$$Q(jk) = \int_{4\pi} q(jk,\theta)d\omega \tag{2.51}$$

$$Q(jk) = 4\pi q(jk, 90°)\left(1 - \frac{P}{3}\right) \tag{2.52}$$

This equation states that the effective cross section can be obtained if one measures the differential cross section at 90°. In our work, we use a diffraction grating to measure radiation at this angle.

The sensitivity of an optical detector may depend on the polarization of the radiation as well as the wavelength. We define $k_{\parallel}$ and $k_{\perp}$ as the detection efficiencies for polarized radiation with parallel and perpendicular electric fields, respectively, to the entrance slit of a monochromator (as in our experiment) that leads to some photon detecting system. Clout and Heddle [42] have shown how to eliminate instrumental polarization for measurements. We consider radiation that is observed at an angle θ to the electron beam axis and also at angle α to the plane of the electron beam. The state indices j and k will be omitted for

simplicity; the expression for the signal, $S(\theta, \alpha)$ that is measured, is given as:

$$S(\theta,\alpha) = \mathcal{I}_{\parallel}(k_{\parallel} cos^2\alpha sin^2\theta + k_{\perp} sin^2\alpha sin^2\theta) + \mathcal{I}_{\perp}[k_{\parallel}(sin^2\alpha + cos^2\alpha cos^2\theta) + k_{\perp}(cos^2\alpha + sin^2\alpha cos^2\theta)] \quad (2.53)$$

Appropriate values of α and θ will greatly simplify this expression. If we choose $\theta = 90°$ and $\alpha = 90°$, so that radiation is observed orthogonal to the electron beam axis with a plane of detection also orthogonal to the plane of the electron beam, then the equation reduces to

$$S(90°, 90°) = \mathcal{I}_{\parallel} k_{\perp} + \mathcal{I}_{\perp} k_{\parallel} \quad (2.54)$$

In this experiment, we assumed that the radiation due to electron-biomolecule collisions had no polarization, i.e., $P = 0$, due to the random orientation of the constituent molecules of the thermally sublimated molecular beam. This means that $\mathcal{I}_{\perp} = \mathcal{I}_{\parallel} = \mathcal{I}_s$, and the signal that is measured, $S(90°, 90°)$ can be shown to be proportional to the effective cross section $Q(jk)$.

$$S(90°, 90°) = (k_{\perp} + k_{\parallel})\mathcal{I}_s \quad (2.55)$$

$$S(90°, 90°) = \frac{(k_{\perp} + k_{\parallel})J(jk, 90°)}{2} \quad (2.56)$$

$$S(90°, 90°) = \frac{(k_{\perp} + k_{\parallel})n(g)Iq(jk, 90°)}{2e} \quad (2.57)$$

$$S(90°, 90°) = \frac{(k_{\perp} + k_{\parallel})n(g)IQ(jk)}{8\pi e} \quad (2.58)$$

Rearranging now for $Q(jk)$:

$$Q(jk) = \frac{8\pi}{(I/e)n(g)} \frac{S(90°, 90°)}{(k_{\perp} + k_{\parallel})} \quad (2.59)$$

If one were to compare unpolarized emissions, then some standard or well-known $Q(jk)_{std}$

can be used to absolutely determine the $Q(jk)$ in question, assuming current and target density have been normalized to be the same for both the target and the standard target:

$$\frac{Q(jk)}{Q(jk)_{std}} = \frac{S(90°, 90°)}{S(90°, 90°)_{std}} \left[\frac{k_{\perp std} + k_{\parallel std}}{k_{\perp} + k_{\parallel}} \right] \tag{2.60}$$

This procedure can be performed to obtain absolute cross section measurements for a transition. This was used in earlier work with pyrimidine [8] where absolute data for Lyman-α production was obtained by comparing with known data for Lyman-α production from H_2.

In this work, absolute cross section measurements were not possible as the vapour pressure of the molecular beam could not be measured, nor could we pass a calibrating gas through the capillary tube of the oven that was used to sublimate the biomolecule sample targets.

Despite this, Equation 2.59 indicates that the current of the electron beam must be measured simultaneously as measurements are made on the cross section during excitation studies. Without correcting for the electron beam current for a given excitation study, measurements made on the relative emission cross section are incomplete.

Additionally, the vapour pressure is not expected to deviate greatly once a steady-state temperature is achieved for the oven. A brief discussion of the steady-state temperature behaviour of the oven is given in Chapter 3.3 while the relationship between the temperature of the sample target loaded in the oven and the corresponding vapour pressure is described in Appendix B. Significant changes in the measured signal of the emission cross section, i.e., excitation function, across the utilized energy range are therefore expected due to the electron beam current, which were corrected for in this work by dividing the measured photon flux signal $S(90°, 90°)$ by the electron beam current, I.

During measurements taken across a spectral range, the electron beam current is still measured despite using a constant electron impact energy for such measurements. For spectral scans, the electron beam current remains constant and so the signal is not expected to

deviate in a significant way due to the electron beam current.

Chapter 3

Experimental Apparatus

3.1 Introduction

Electron collisions are performed inside the main chamber kept under a vacuum of 3 to 5×10^{-7} Torr. Inside this chamber, an electron beam collies with a beam of sublimated target molecules at right angles. Excited atomic and ionic species resulting from this collision spontaneously emit radiation in all directions. The main chamber is connected to a half-metre Seya-Namioka VUV spectrometer which intercepts the resultant radiation that is mutually orthogonal to the crossed beams. The diffraction grating in the spectrometer allows different wavelengths of radiation to be picked out and sent to a photon detection apparatus.

The experimental apparatus was designed to accommodate two modes of data acquisition. In the first mode, the electron beam is kept at a constant energy of 100 eV while timing electronics rotate the diffraction grating inside the spectrometer to measure the intensity of radiation over an arbitrary wavelength range. During such measurements, the wavelength could sweep from 80 nm to 140 nm. The second mode of data acquisition instead keeps the diffraction grating fixed on one wavelength but allows the electron beam to vary in energy while measuring the intensity of the radiation. This allows us to acquire a so-called "excitation function", the plot of photon counts of a fixed wavelength against the electron

impact energy. The excitation function can be related to the cross section for the transition being observed. The electron beam's energy can vary from 0 eV to 400 eV for this mode of measurement.

Both modes of data acquisition are used for these collisional experiments. The first method, where the diffraction grating is rotated to sweep across an arbitrary wavelength range, is used to determine the sort of transitions that are occurring and to link these radiative transitions with species that are relevant, i.e., the possible fragments from the collision. After identifying radiative transitions over the wavelength range, the second method is employed to acquire the excitation function. Data was acquired by a Multi-Channel Scaler (MCS) program on a computer, which would bin data from the detection electronics.

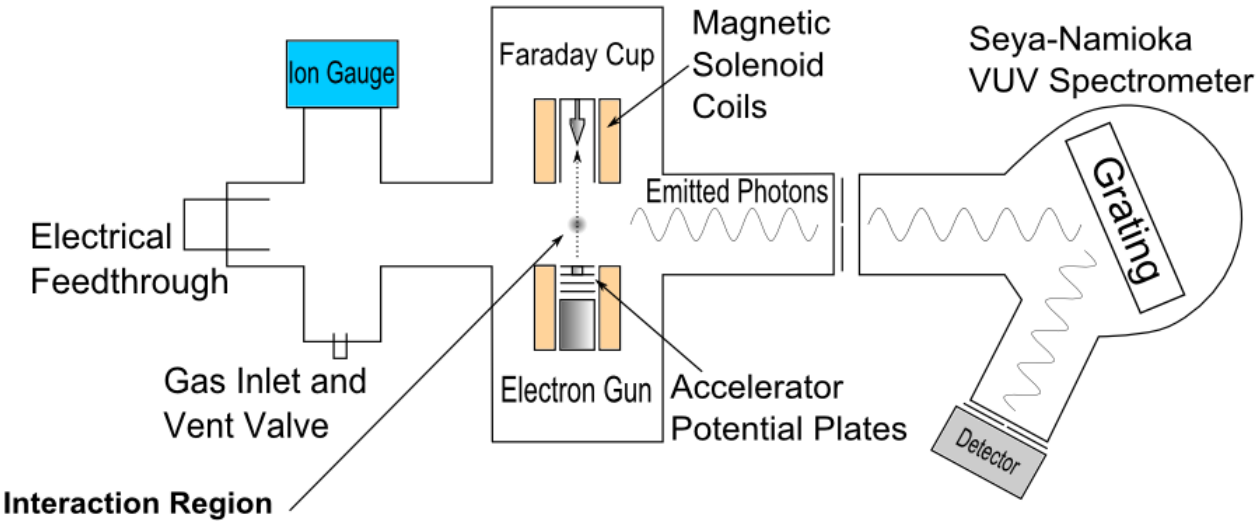

Figure 3.1: An overview of the experimental apparatus. Key features are the interaction region in the centre of the chamber, where a target sample is sublimated from an oven inside and crossed with an electron beam that is emitted from the electron gun. The molecular beam is shown in the centre of the interaction region and is oriented out of the page. The photons that emit at right angles to both beams enter the VUV spectrometer. A diffraction grating picks out the wavelength of light that enters the detector.

Figure 3.1 provides an overview of the main experimental apparatus, which includes the electron-collision chamber, the VUV spectrometer, and the photon detection arm. The ion gauge is used to measure the pressure of the chamber, while the gas inlet valve is used to fill

the chamber to an approximate pressure of 5×10^{-5} Torr with a gas used for calibration. The electrical feedthrough is a flange that allows power supplies from outside the chamber to be connected to resistive wiring that is wrapped around an oven in the centre of the chamber and around the Faraday cup.

3.2 Vacuum Chamber

The main vacuum chamber is made of stainless steel and consists of three pairs of mutually orthogonal ports. Each port has a diameter of 8" and is sealed by a Viton O-ring. The entire apparatus is evacuated with roughing pumps connected to the system with Kwik-Flange™ ISO KF stainless steel tubes and valves. An Edwards E2M12 vacuum pump is attached to the main collision chamber and an Edwards Speedivac ED100 is attached to the VUV spectrometer. The roughing pressures are measured by a Kurt J Lesker KJL 6000 Thermocouple Gauge and a Granville-Phillips Series 340 Vacuum Measurement Controller for each of these roughing pumps respectively. The chamber's pressure is reduced to about 20 mTorr with these roughing pumps, which is necessary for the efficient operation of turbo pumps that further reduce the pressures inside the main chamber.

Two turbo pumps are used in conjunction to quickly acquire a low background pressure in the chamber. A Varian TV 701 Navigator turbo pump is fastened underneath the spectrometer chamber and is typically operated at 28 kRPM. A Varian Turbo-V1000 turbo vacuum pump is attached underneath the electron collision chamber. Operating background pressures were 3 to 5×10^{-7} Torr. If a gas was introduced into the chamber for a study, the pressure was maintained on the order of 10^{-6} Torr or a low 10^{-5} Torr. These pressures were measured by a Veeco RG1000 Ionization Gauge, which is mounted to a supplementary compartment of the main chamber.

The sample oven is perched inside the main chamber directly above the Varian Turbo-V1000 turbo vacuum pump in a stainless steel cradle. The sample target is loaded into the

oven and is heated to create a sublimated molecular beam that diffuses upwards to the top of the chamber, which is sealed by a plain flange. Most of the sample's beam deposits on this top flange but some of the sample deposits on the sides of the chamber.

An electron gun and Faraday cup are situated opposing each other as is shown in Figure 3.2. Their mutual axis is perpendicular to the axis of the molecular beam sublimated from the oven. An electron beam produced by the electron gun intercepts the molecular beam orthogonally and radiation is produced from the collisions between the electrons and the sublimated sample. This radiation is measured by the detection arm after it passes through the VUV spectrometer system.

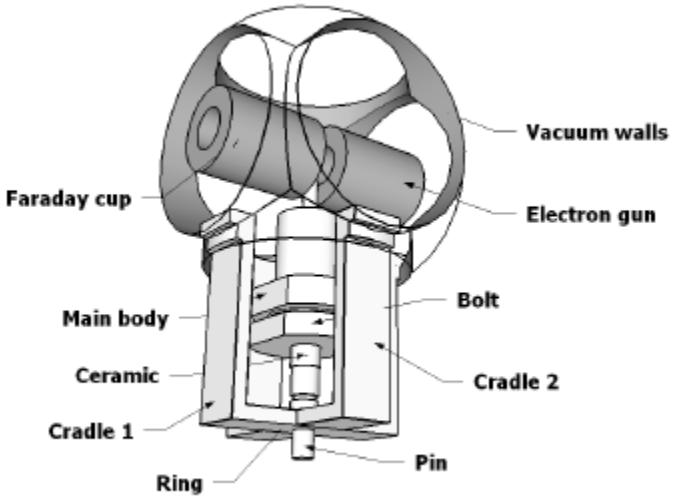

Figure 3.2: A representation of the main chamber provided by Jeff Hein. The oven sits on a ceramic piece that is fixed on two interleaved stainless steel cradles, which are held up by the sides of the chamber. The sample is heated in the body of the oven where it diffuses out as a beam from the stem and intercepted with the electron beam.

The electrical components of the Faraday cup, electron gun, and biomolecule oven are all connected to external power supplies via feedthroughs in a number of the mounting flanges. Resistive wiring wrapped around the oven and Faraday cup is connected to Variac power supplies outside the chamber. There is also a thermocouple connected via this same mounting flange to measure the temperature of the oven's stem and the oven's main body.

A gas inlet system with a needle-nose valve allows low pressure calibration of gases to be introduced into the main chamber. Additionally, it is often used as a vent to bring the pressure of the chamber to atmospheric pressure so that the chamber may be cleaned or to reload the oven.

3.3 Biomolecule Oven

The biomolecule oven, as pictured in Figure 3.3, is a stainless steel barrel and outfitted with an array of capillary tubes in its stem. The oven's body is sealed by a removable metal plug situated on a threaded base-bolt on the bottom. The sample is loaded into the oven from the bottom before the oven is inserted into the chamber which is then vented and kept under vacuum. Aerorod heating wire is wrapped around the oven's 1" diameter body and 0.25" diameter stem and connected to a Variac AC supply outside the chamber via an electrical feedthrough. The Variac supply provides current to the heating wire to warm the oven. When enough heat is supplied to the sample inside the oven, the sample sublimates and the oven emanates a molecular beam vertically upwards..

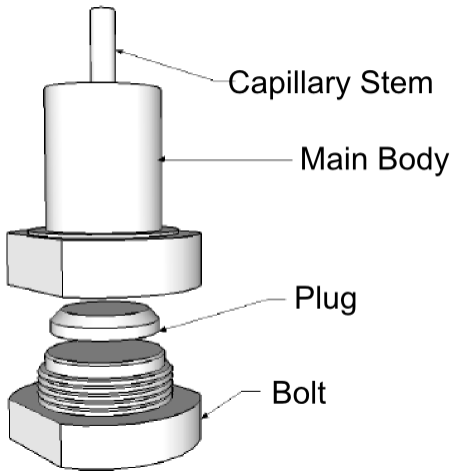

Figure 3.3: The components that make up the oven. A sample is loaded through the body, which is sealed by the plug. The bolt base is threaded into the bottom of the oven. Representation provided by Jeff Hein.

The main body is typically maintained around 170°C to 190°C . The capillary tube is kept at a higher temperature than the body to prevent clogging in the tube and is about 50°C higher than the body's temperature. The Variac supply typically supplies 35 V to 40 V to heat the oven to temperatures that will sublimate the sample.

A thermocouple is attached to the oven's stem and to the oven's body, and it is wired through an electrical feedthrough to outside the chamber. The wiring connects to a switch box and a multimeter to display the temperature. The switch box allows selective monitoring of the oven body's temperature or the oven stem's temperature.

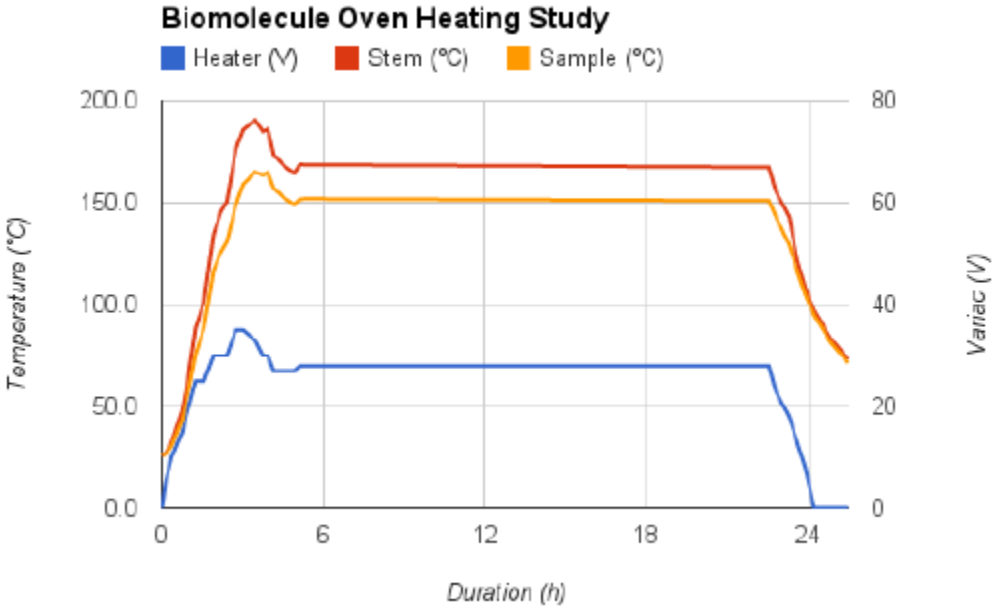

Figure 3.4: An oven heating study. The blue line indicates the voltage of the heater, and its appropriate units are on the right axis. The orange line indicates the oven body temperature and the red line indicates the oven stem temperature. The units for temperature are indicated on the left axis.

An oven heating study is shown in Figure 3.4. In it, the voltage of the Variac power supply for the heater was allowed to vary and the corresponding temperature of the oven's body and the oven's stem were recorded. During this study, the oven was empty. The oven was heated from room temperature and as can be seen in Figure 3.4, the temperature of the body and the stem reaches a steady-state well by the 6 hour mark and remains constant until

much later when the the power supply is turned down. At a voltage of about 30 V, the oven's body reaches 150 °C while the stem reaches a steady-state of about 175 °C . The temperature at which the oven is held is related to the vapour pressure of the sublimated molecular beam in an exponential fashion—small deviations in the oven temperature can drastically affect the vapour pressure of the beam. The oven must be held at steady temperatures during data-taking for a consistent molecular beam vapour pressure. A discussion on this relationship is given in Appendix B where estimations of the vapour pressure for thymine and adenine are provided for temperatures relevant to this experiment.

3.4 Electron Beam System

The electron gun supplies a magnetically collimated monoenergetic beam of electrons from a tungsten filament along an axis othogonal to the molecular beam. The beam enters the Faraday cup, a positively biased metal needle on the other end of the chamber, and the current to the Faraday cup is measured by a picoammeter.

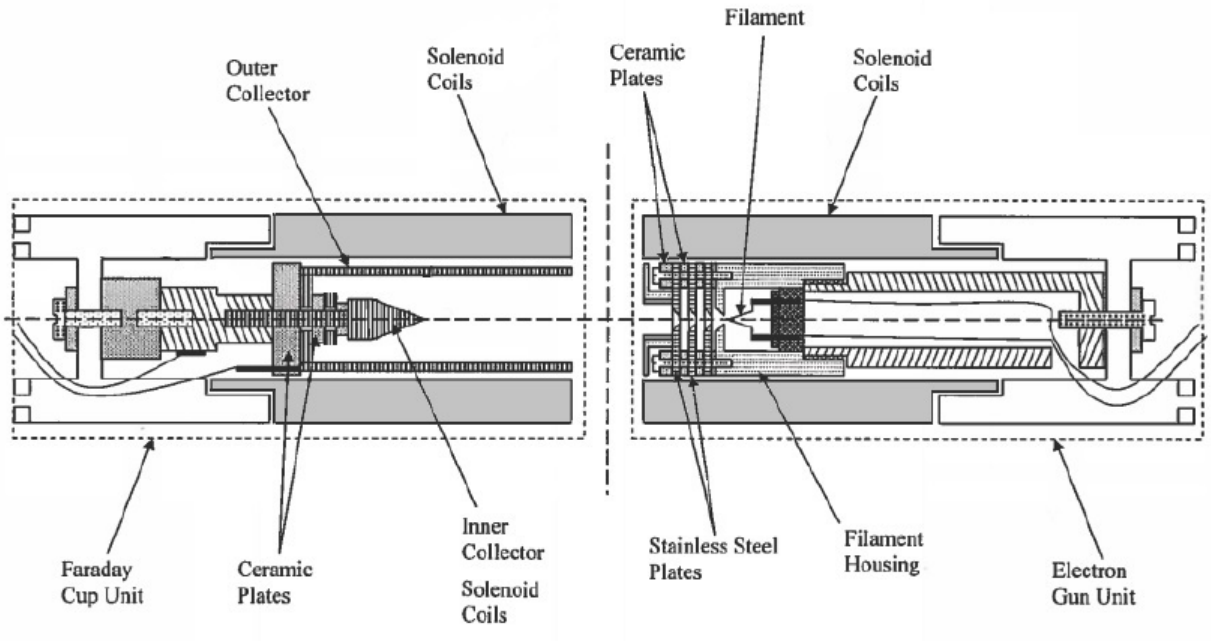

Figure 3.5: The electron gun and Faraday cup units. Reproduced from Abdellatif [3].

During spectrum measurements, the gun energy was kept at a constant 100 eV. During excitation measurements, the gun energy was ramped from 0-400 eV by the ramping power supply. The MCS program on the computer could not only bin data during measurements but could also direct the ramping power supply to supply a specific energy range for the electron gun. An initial energy to begin an excitation scan, a final energy to end it on, and the energy resolution per channel could all be specified in the MCS. During excitation measurements, the gun was increased by 0.5 eV per channel.

The tungsten filament for the electron gun is manufactured by Soquelec and sits on a ceramic base, which itself is mounted on a stainless steel tube, as seen in Figure 3.5. This mounting tube has threading on its top where the filament sits so that a filament housing can be secured over the mounted filament. The filament housing is a stainless steel covering with three electron lens plates that are independently supplied with voltage from a power supply. The lens plates are interleaved with ceramic pieces and fastened to the filament housing by screws secured through the ceramic pieces. The bottom of the mounting tube has a screw aligned along its longitudinal axis that is inserted into an outer chassis and the filament-lens conglomerate is tightened to the outer chassis by a nut. The outer chassis is screwed into a flange. Three electrically insulating but thermally conducting washers separate the outer chassis from the mounting tube and allow heat from the hot filament to dissipate. A magnetic solenoid coil is placed around the filament housing and mounting tube to help collimate the electron beam.

The Faraday cup sits on the opposite side of the chamber from the electron gun and consists of a stainless steel needle biased up to 50 V and an earthed outer cup. The needle head, which is also called the inner cup, has a threaded base that is inserted through a hole at the bottom of the outer cup and suspended by a ceramic sheath to avoid direct electronic contact with the outer cup. The threaded base is partly wrapped with Kapton tape as an additional measure to avoid electronic contact between the cups. The thread base of the inner cup is fastened to a cylindrical mount which is then connected to the Faraday cup's

outer chassis with a screw through a threaded ceramic piece.

A power supply is used to keep the current through the tungsten filament at 2.20 A to 2.30 A, as this results in a current of about 50 μA across the Faraday cup. The body of the filament housing, in conjunction with the sequential two plates, form an Einzel lens; this focuses the beam while also accelerating it. The third lens, at the tip of the gun, is grounded to shield the beam from external fields. Electrons are thermionically emitted from the tungsten filament and accelerated by the lens plates. The filament housing and the plates held at a bias separately from the filament and are wired to adjustable resistors so that the voltage across the plates can be changed. This is done because it affects the focusing of the beam; when the gun is operational under vacuum, the voltages across the plates are adjusted to optimize the current through the Faraday cup.

The electrons attracted to the positively biased needle are passed to ground via a picoammeter that measures the collected current. Currents could range from 40 μA to 100 μA. The inner cup was positively biased to stop electrons from being back-scattered into the interaction region. The picoammeter is also connected to a Voltage-to-Frequency (V-to-F) converter; this device outputs a signal to a port on the computer to the MCS program that is proportional to the current measured by the picoammeter. In this way, the current behaviour can be measured along with the ramping energy of the ramping power supply and divided from the acquired excitation function.

Figure 3.6 shows the electronics circuitry for the electron gun and Faraday cup. A switch controls the choice of power supply for spectrum measurements (Constant Energy supply) or for excitation measurements (Ramping Energy supply). Also pictured is the lens supply to optimize the current in the chamber. The cathode is connected to the filament supply near the lenses. The Faraday cup is shown connected to its bias and a switch controller that allows one to measure the current across the inner cup or the outer cup with the picoammeter.

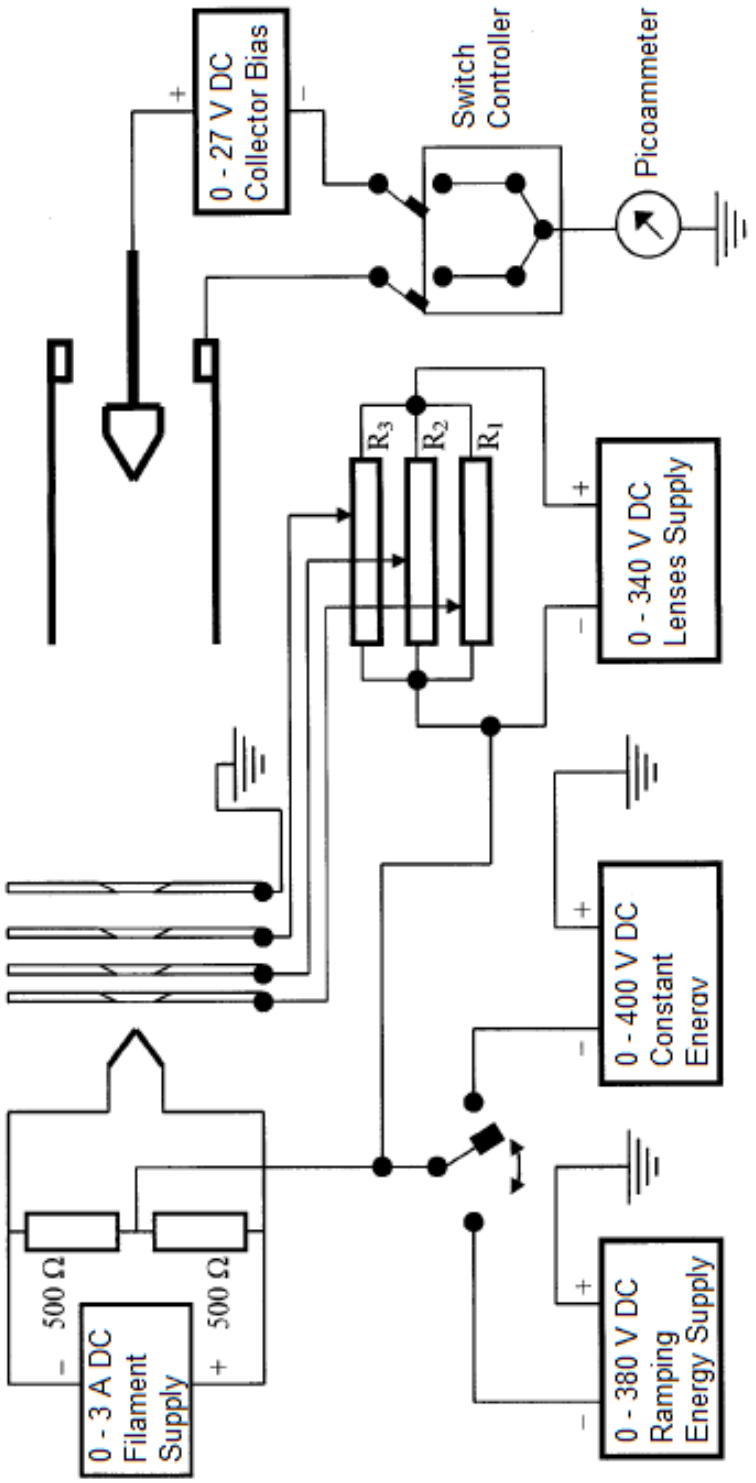

Figure 3.6: The circuitry for the electron gun and Faraday cup. Reproduced from [3].

3.5 VUV Spectrometer

A McPherson 1/2 m Seya-Namioka Vacuum Ultraviolet (VUV) spectrometer is connected to the main chamber by one arm and connected to the detector system on the other arm. Radiation from the main chamber that is orthogonal to the crossed-beam system travels through an adjustable entrance slit into the spectrometer to a diffraction grating. The diffraction grating is rotated by a stepper motor so that a chosen wavelength of light is directed through an exit slit so that it is detected by the channel electron multiplier (CEM) or photomultiplier (PMT).

A slit and shutter mechanism is included at the end of each arm of the spectrometer to collimate light. The slits are adjustable and provide up to a 2 mm opening and can be adjusted in increments of microns. During spectrum measurements, where resolution is critical to distinguish features, the slits are kept at 0.2 mm which results in 0.8 nm at full width half maximum (FWHM) for a feature. During excitation measurements, where intensity is more important than resolution, the slits are opened to 1 mm.

The diffraction grating in the VUV Spectrometer has 2400 lines/mm and is rotated on a Seya-Namioka mounting by a stepper motor. On the instrument, there is a counter that linearly corresponds to the rotation of the grating. A gas like He, H_2, or N_2 with well-studied features is used to calibrate the counter reading on the instrument with the wavelength of radiation.

The stepper motor is responsible for the rate of rotation of the diffraction grating. It rotates a finely threaded shaft in discrete steps. A threaded block envelopes the threaded shaft; rotation of the shaft causes the block to translate along the shaft. This block is connected to a mechanical gear system that rotates the diffraction grating inside the vacuum, which in turn is connected to a counter dial. The stepper motor is controlled by a BNC555 unit, and each pulse from this unit instructs the stepper motor to turn one step corresponding to 1/8th of a full turn on the counter.

The vacuum inside the spectrometer was kept at 10^{-7} torr to minimize degradation of

the spectrometer's reflection efficiency.

3.6 Photon Detection System

A Burleigh CEM model 4028 was used to detect radiation in the VUV range of 50 nm to 150 nm and was supplied with 3.2 kV from a Ortec model 569 Bias Supply. The CEM was coated with CsI so that it had greater sensitivity at higher wavelengths.

The CEM produces pulses that are sent through signal processing electronics arranged on a NIMbin. A pulse is first sent to a preamplifier and then to the Ortec 474 Timing Filter Amplifier (TFA) which amplifies and shapes the signal. The pulse is sequentially sent to the Ortec 584 Constant Fraction Discriminator (CFD) to minimize recorded noise. The output from the CFD is sent to the Ortec 775 Counter and to the Multichannel Scaler (MCS) on the computer. The MCS hardware is a card attached to the inside of the computer with BNC ports for multiple uses. Spectrum scans and excitation scans are recorded using the MCS-32 software and are saved as MCS files and as ASCII files. Figure 3.7 illustrates this sequence.

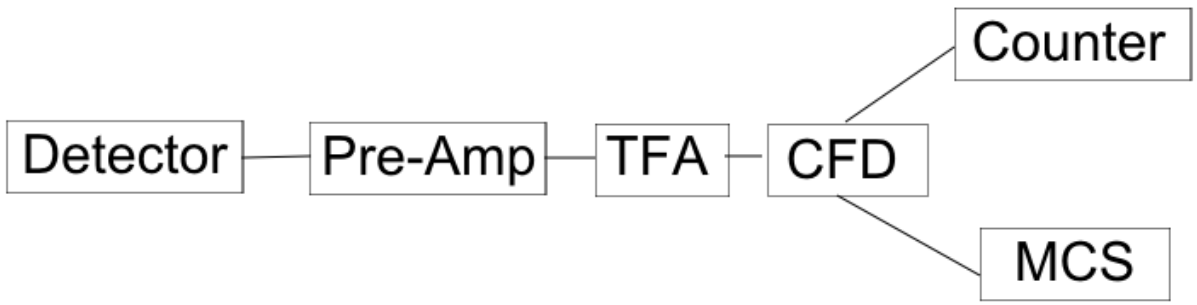

Figure 3.7: A block diagram of the electronics sequence for data collection. The signal is sent to an electronic counter device and to the MCS simultaneously.

The detector housed inside the detection arm of the vacuum chamber is connected to a small box external from the chamber. The circuit diagram for this box is given in Figure 3.8, which links the detector inside the chamber with both an adjustable 3 kV power supply

and the Pre-Amp. The 3 kV power supply directly supplies the detector with voltage for its operation to develop a signal, which itself is passed on to the Pre-Amp and the rest of the signal processing electronics as indicated in Figure 3.7.

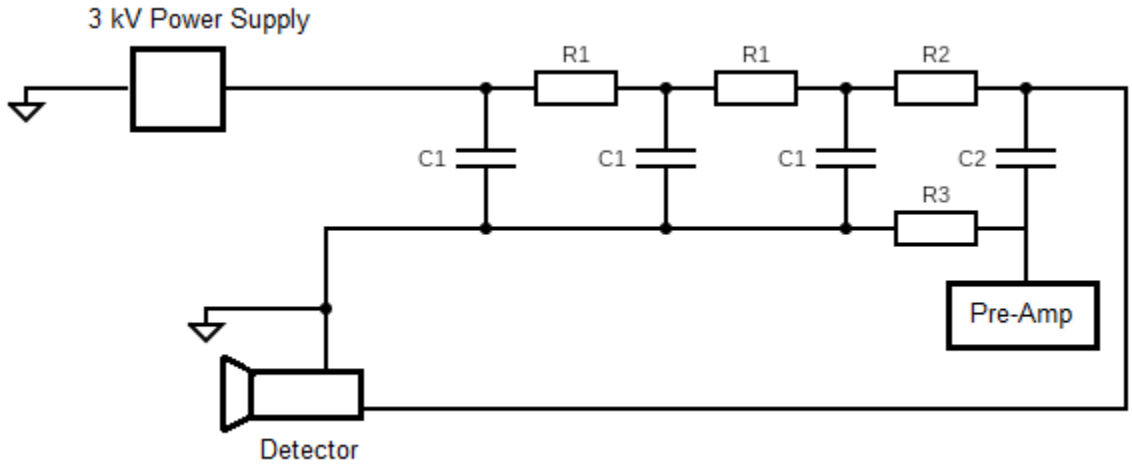

Figure 3.8: The circuit for the detection box. The triangles in this diagram indicate ground.

3.7 Timing System

A BNC 565 Pulse/Delay Generator was used during spectrum measurements to create a pulse sequence that controlled the stepper motor and instructed the MCS program to collect and bin data appropriately. During spectrum measurements, the BNC565 unit sends a pulse to a control box, which in turn sends the pulse to the stepper motor. Each pulse causes the stepper motor to rotate the diffraction grating in equal increments. This rotation corresponds to the counter reading on the spectrometer - each discrete turn by the stepper motor increases the counter by a factor of 1/8. The counter reading corresponds to a sweep over wavelengths - when the counter reading increases by 1, the spectrometer has sweeped over 0.5 nm. This means that 8 pulses must be sent by the BNC565 unit to rotate the stepper motor by 1 on the counter and therefore sweep over 0.5 nm.

Figure 3.9 illustrates the timing logic of the pulse system for a spectrum scan. Channel A

of the BNC565 unit sends an initial pulse at t_0 to the MCS, instructing it to begin recording data. At t_1, Channel C sends a pulse to the stepper motor so that the spectrum measurement begins on the initial counter reading, c_0. Channel C then sends pulses in equal intervals of Δt to the stepper motor. Once the counter has increased by 1, to c_1, a pulse sent by Channel B collects the data and records it in the first bin, Ch_0, of the MCS software.

Before a spectrum measurement is performed, a time T, called the dwell time, is decided for the width of each bin. A dwell time of 60 s was typical for spectrum measurements. Δt corresponds to 1/8th of the dwell time; this Δt was typically 7.5 s. A sweep over some interval of wavelengths, along with the dwell time, would be decided before a scan. This would instruct the number of bins to use in the MCS software and for the counter sweep for the spectrometer. This would be performed after using a calibration gas to relate the counter reading to wavelength.

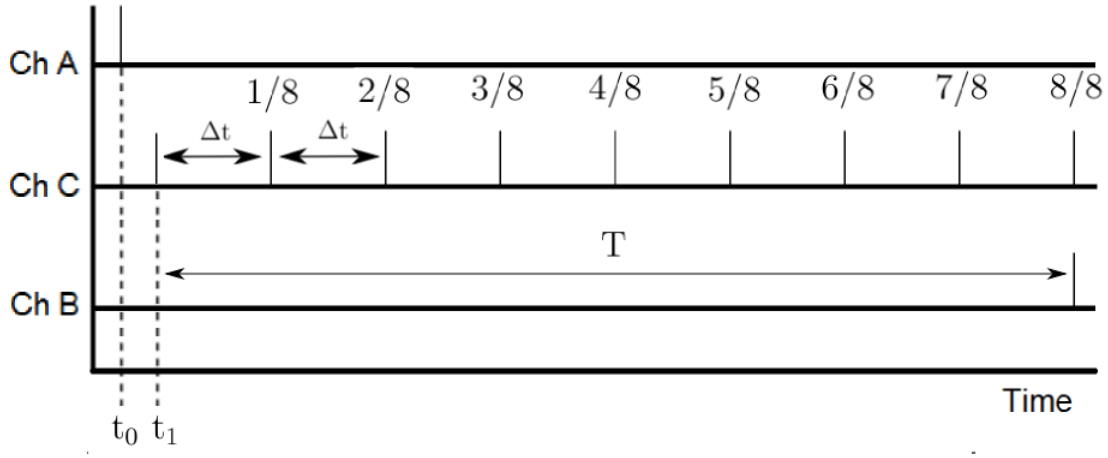

Figure 3.9: Timing diagram for spectrum measurements. Channel A corresponds to the initiating pulse. Channel C corresponds to the pulses sent to the stepper motor to rotate the diffraction grating. Channel B corresponds the times in which data was binned. The separation time between Channel C pulses, Δt, is 1/8th of the dwell time, T. Note that Δt is not the difference between t_0 and t_1—the interval between these t_0 and t_1 is 100 μs and has been exaggerated for this diagram.

The control box for the stepper motor can receive pulses from the BNC565's Channel C and pass them along to rotate the diffraction grating during spectrum measurements, but it was also capable of controlling the stepper motor manually. However, the control box was

only used in this way outside of taking measurements as a convenient tool to manually reset the entire counter sweep or to rapidly advance the stepper motor to a desired wavelength setting.

As the finely threaded shaft for the spectrometer is of finite size, a safety switch for the stepper motor was implemented and connected to the control box. This prevents the stepper motor from causing the mechanical gear system to exceed the physical length of the shaft and damage the system. The safety switch is a button located near the end of the shaft - once the block translates to this threshold on the shaft, it triggers the button which interrupts the circuit and prevents the stepper motor from receiving pulses from the control box.

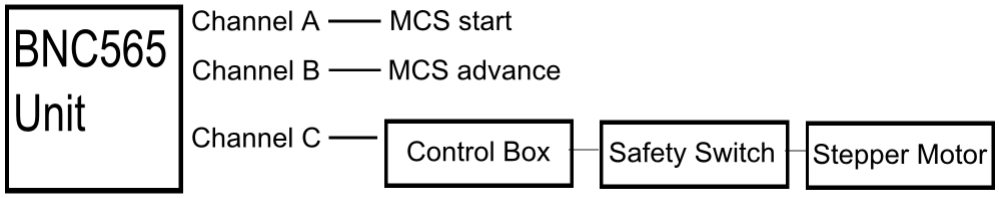

Figure 3.10: Block diagram for pulsing process during spectrum measurements. Channel A instructs the MCS program to begin. Channel B instructs the MCS program when to bin data. Channel C advances the stepper motor through the control box.

During excitation measurements, the MSC program uses its own internal clock system to bin data. Additionally, the MSC software is used to control the ramping supply on the NIMbin. An initial voltage and a final voltage is entered into the software along with the total number of bins for the data. The MCS software instructs the ramping supply to increase by equal increments until it reaches the voltage limit input, and to bin each data according to a dwell time input. Excitation scans were typically done with 0.5 eV per bin for 60 s each. As a complete excitation measurement could be performed relatively quickly (about 2 hours), the MCS software was instructed to restart the scan at the initial energy and begin another pass across the energy range. The data from the new pass would be added together with the previous pass; this would go on until the software had finished all of its passes and the final excitation scan is the total sum of the signal from each pass.

3.8 Overview

Figure 3.11 is a block diagram of the entire experiment featuring the main components of the system.

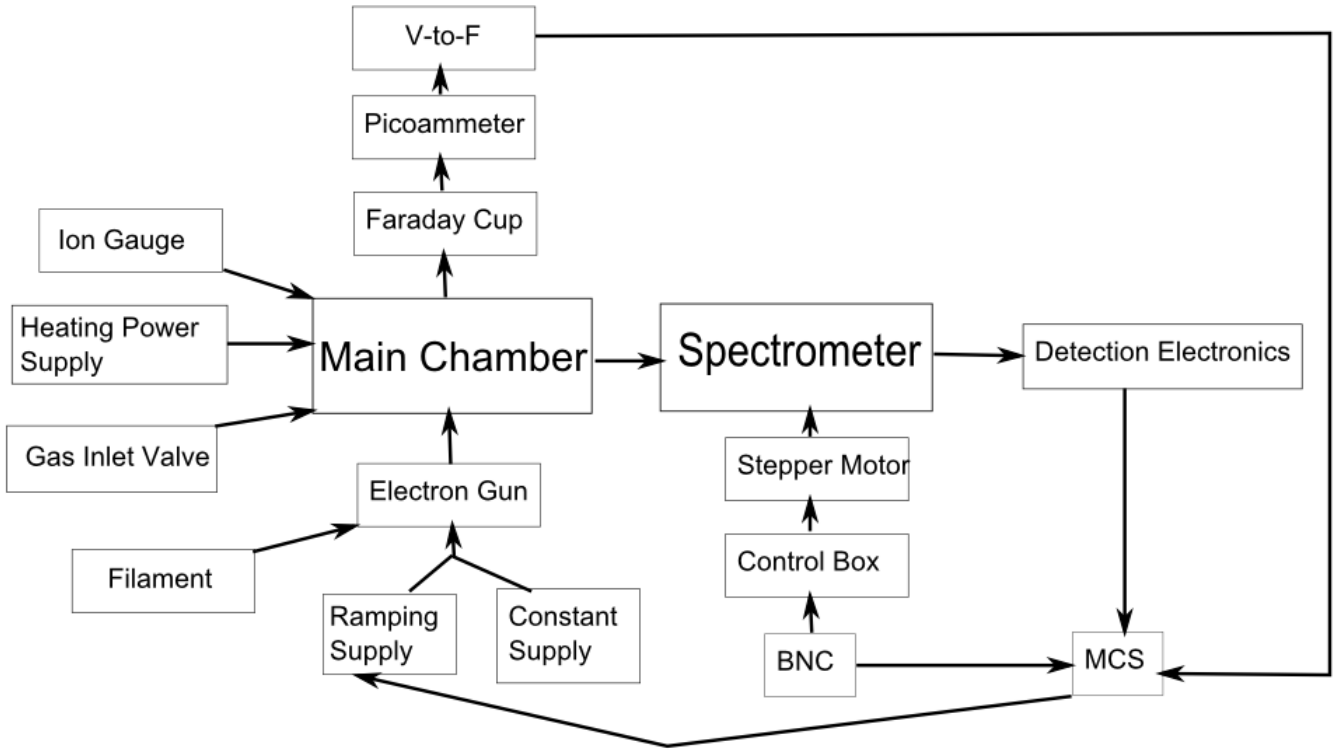

Figure 3.11: A block diagram overview of the main components of the experiment.

Chapter 4

Electron Impact Studies on Thymine

4.1 Overview

Thymine was the first target for these crossed-beam studies using the stainless steel oven. Figure 4.1 is a diagram of the molecule's geometry. Reagent grade thymine was loaded into the oven and was sublimated from the stem of the oven so that it could be intercepted by the electron beam. The body of the oven was kept heated at temperatures between 150°C and 160 °C while the stem was kept about 20°C higher to prevent clogging. The work of Rahman et al. [43] suggests that at these operating temperatures the vapour pressure in the oven should be less than 5 mTorr.

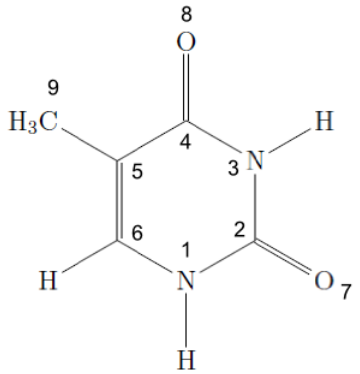

Figure 4.1: The molecular geometry of thymine.

Two kinds of experimental data were taken. Firstly, the emission spectrum of thymine was measured over the wavelength range of 80 to 150 nm while the energy of the electron gun was fixed at 100 eV. Secondly, the intensity of a spectral feature in the emission spectrum was measured as the energy of the electron gun was allowed to change from 0 eV up to 430 eV.

The electron beam current was kept constant at 50 μA for the spectrum measurements and was measured simultaneously with the measurements made on photon emission; no significant deviation in current was observed during these measurements. The energy resolution of the electron beam was about 1 eV at full-width half maximum. Photon fluxes were assumed to be unpolarized due to the size and complexity of the thymine molecule. Unfortunately, as there was no capability to measure the pressure in the thymine beam, the cross section could not be measured in absolute terms.

4.2 Thymine Photoemission Spectra

Figure 4.2 is the measured emission spectrum taken of thymine using a fixed electron beam energy of 100 eV. The detector used in this experiment, along with the diffraction grating, have a variable efficiency across the wavelengths. The data has been corrected to account for this variation in detection probability; a full description for this correction procedure is discussed in Appendix C.

As evident from the figure, the Lyman series of hydrogen dominates the spectrum. Carbon, nitrogen, and oxygen do not contribute a significant share to the signal; if the features are present, they cannot be discerned from the noise. The dominance of H over C, N, or O should not be surprising. All the H are exocyclic and can be extracted by breaking one of the four C-H bonds (three of which belong to the methyl group) or one of the two N-H bonds. Breaking off either of the O and exciting them should be less likely than extracting a H fragment as there are less sites for an impact on O to occur. Extracting the C from

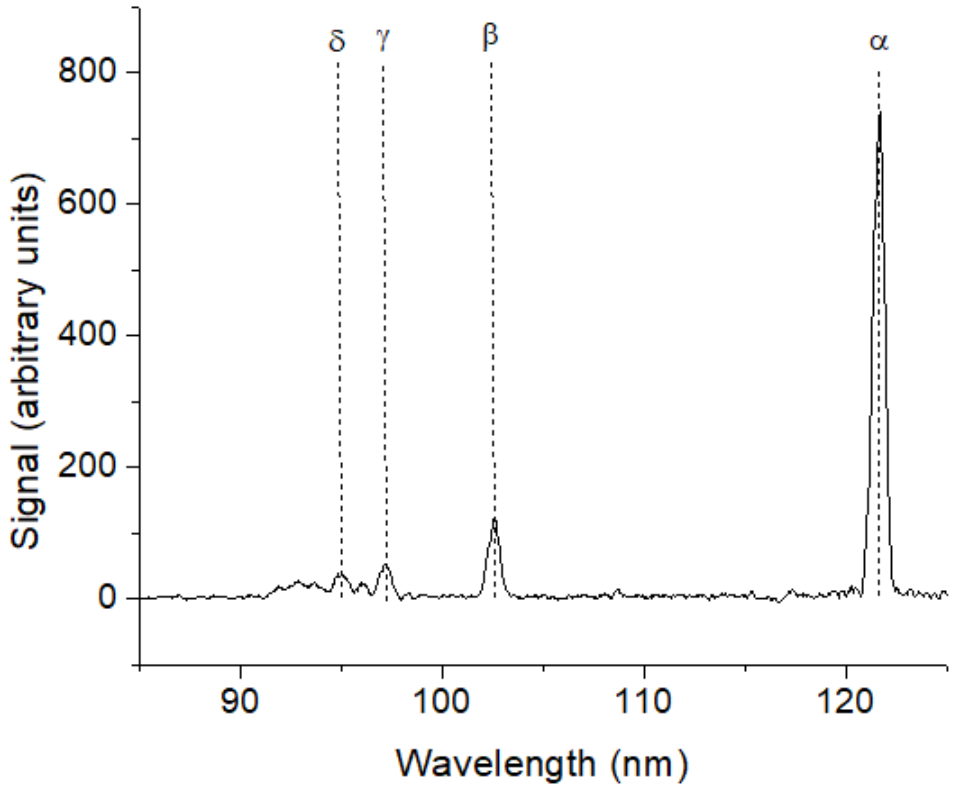

Figure 4.2: The emission spectra of thymine measured from 85 nm to 125 nm with a fixed electron beam energy of 100 eV. Entrance and exit slits were kept at 0.2 mm to reduce spectral width. The data have been corrected to take account of the spectral response of the detection system.

the methyl group would require 3 H to be stripped from it, and extracting any endocyclic C would require a significant breach upon the ring structure. Similarly, the extraction of N would also require a breach of the ring. However, as will be discussed later, these are not the only fragmentation processes that can occur and yield an atomic fragment, but the dominance of the Lyman series over the wavelength range considered should be expected. Additionally, comparison with electron mass spectrometry work by Imhoff et al. [31] show that C^+, N^+, and O^+ ions contribute very little to the total mass spectrum, less than 1%, whereas both H^+ and $H_2{}^+$ were more prominent. Thus, excited H-atom production is to be expected also.

Table 4.1 indicates the possible non-hydrogen features and the corresponding transitions

Atomic fragment	Wavelength (nm)
O I	87.8
O I	98.9
O I	104.1
O I	115.2
O I	130.4
C I	126.6
C I	127.8
C I	136.4
N I	120.4
N I	125.3

Table 4.1: Relevant non-hydrogen atomic features that could be observed from thymine. Taken from NIST[1].

in the 85 - 125 nm range of the spectra that might have been observed during measurements. Outside of this range, the strong 151.6 nm and 165.8 nm features of C could not detected because of a lack of spectral sensitivity at these wavelengths.

Feature	Wavelength (nm)	Transition	Relative Cross Section
α	121.6	H[2p→1s]	1.00
β	102.6	H[3p→1s]	0.16 ± 0.01
γ	97.3	H[4p→1s]	0.08 ± 0.01
δ	94.9	H[5p→1s]	0.05 ± 0.01
...	...	...	...
Lyman limit	91.2	H[∞p→1s]	N/A

Table 4.2: Features present in thymine emission spectrum.

Table 4.2 lists the features that are present in the spectra, namely the Lyman series, along with their cross sections relative to the Lyman α feature at 121.6 nm. The rest of the Lyman series, up to Lyman δ, are all uniquely resolvable, but the hydrogen features that follow blend and merge together until the Lyman series finally terminates at 91.2 nm. These relative cross sections are proportional to the area underneath them. The areas were determined with a Gaussian fit as described in Appendix E. The relative cross sections of α compared to β, α:β, is 1.00:0.16. This is less than the same ratio taken for pyrimidine studies [8], in which this ratio was 1.00:0.19, but greater than the 1.00:0.12 ratio measured

for H_2 from McConkey et al. [44].

Between Lyman-γ and Lyman-δ there is a small background contamination from the (0,0) band of the $c_4{}'^1\Sigma_g^+ \rightarrow {}^1\Sigma_g^+$ of N_2 that was present even in scans taken of the background with a cold oven.

4.3 Excitation Function Studies

The most intense feature in the spectrum of Figure 4.2, Lyman-α, was chosen to measure for an excitation function study. As molecular beam density could not be monitored concurrently with photon flux of the radiation from H fragments, the excitation functions presented here are not shown in absolute terms. Figure 4.3 shows a measurement of this relative cross section from 0 eV to 450 eV. The onset of the cross section begins at 23 $\pm$ 1.0 eV and rises in a gradual manner. Further discussion of the threshold of the relative cross section as seen in Figure 4.5 is given later.

From 60 eV the relative cross section rises to a broad maximum of 160 eV after which it begins to fall off. This slow rise of the excitation function to its broad maximum suggests that at higher energies it goes as $\ln E/E$, which is indicative that dipole, optically allowed, processes are significant according to the Bethe-Born approximation, as discussed in Chapter 2.

To check if the excitation function went as $\ln E/E$, a Fano plot was made from the excitation function in Figure 4.3 and is given in Figure 4.4. In the Fano plot, the horizontal axis is the natural logarithm of the energy, while the vertical axis is the product of the excitation function and energy. This has been discussed directly after Equations 2.30 and 2.32. If the excitation function in Figure 4.3 went on as $\ln E/E$ at high energies, then the Fano plot will appear linear beyond the natural logarithm of the energy that corresponds to the excitation function's peak. As stated previously, excitation function in Figure 4.3 appears to have a broad maximum about 160 eV, which corresponds to about 5.08 for the horizontal

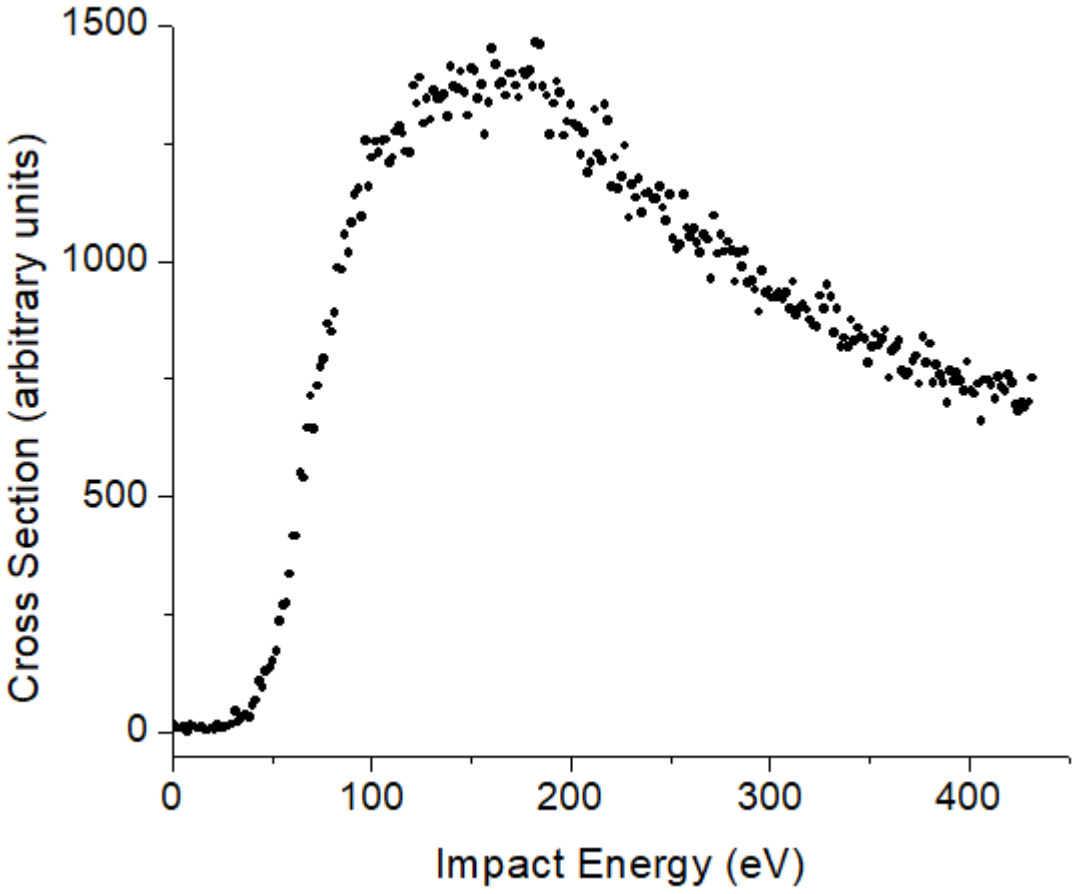

Figure 4.3: Excitation study performed on Lyman-α from 0 eV to 450 eV.

axis of Figure 4.4; it is approximately beyond this point where the linearity of the Fano plot would be of importance. A proper test of the Bethe-Born prediction requires higher energies than what has been used in this work, but the plot indicates $\ln E/E$ behaviour.

The onset threshold energy for the H[2p-1s] transition, at 121.6 nm, was determined from Figure 4.5 by performing a linear fit to the threshold region. As mentioned earlier, this was determined to be:

$$E_t[H(121.6\text{ nm})] = 23.0 \pm 1.0\text{ eV} \tag{4.1}$$

This threshold energy was corrected by using a well-known known threshold energy of a calibration gas, as discussed in Appendix D. Extracting an excited H atom requires the breaking of a C-H or N-H bond in the molecule. Schneider [34] has shown that 3.72 eV is

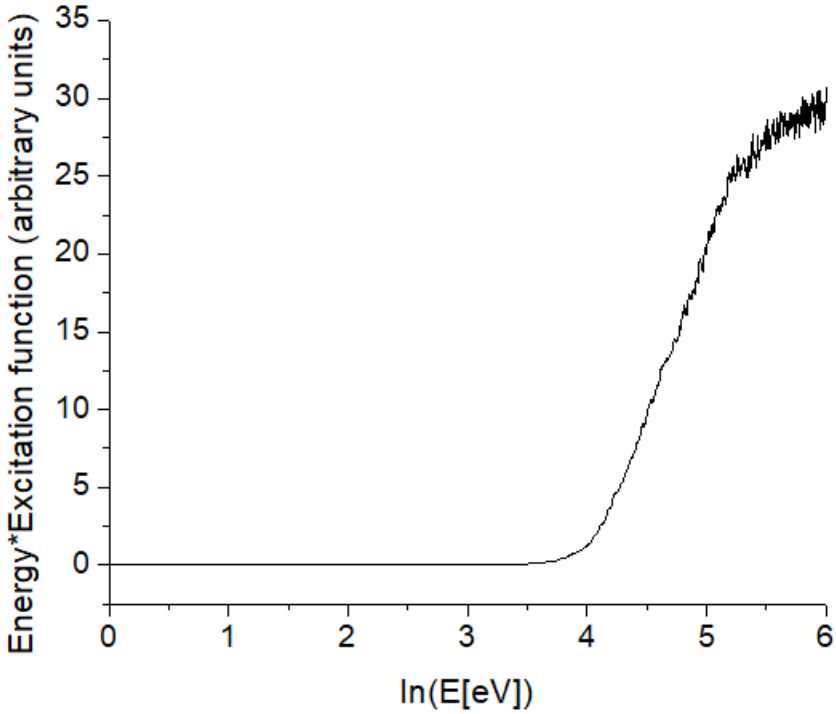

Figure 4.4: A Fano plot taken of the excitation function. The horizontal axis is the logarithm of the energy for the excitation function while the vertical axis is the energy of the excitation function multiplied by the excitation function.

required to break the C7-H bond in the methyl group and release a ground state H atom. Likewise, the C6-H bond requires 4.77 eV. The N-H bonds require 4.08 eV to break N1-H and 5.19 eV to break N3-H. Additionally, 10.2 eV is required to excite the H atom to its 2p state, which suggests the following minimum appearance energies:

$$E_t(C7 - H) = 13.92 \text{ eV} \tag{4.2}$$

$$E_t(C6 - H) = 14.97 \text{ eV} \tag{4.3}$$

$$E_t(N1 - H) = 14.28 \text{ eV} \tag{4.4}$$

$$E_t(N3 - H) = 15.39 \text{ eV} \tag{4.5}$$

If any of these processes were very significant for the formation of Lyman-α photons in the

work, the cross section threshold would begin around these energies. However, the measured threshold is 9.1 eV higher than the most likely threshold as listed above; it is unlikely that such an energy discrepancy could be accounted for in terms of fragment kinetic energies due to repulsive potential surfaces of the parent molecule. Therefore, these processes where only a single H is released from the thymine molecule do not contribute significantly.

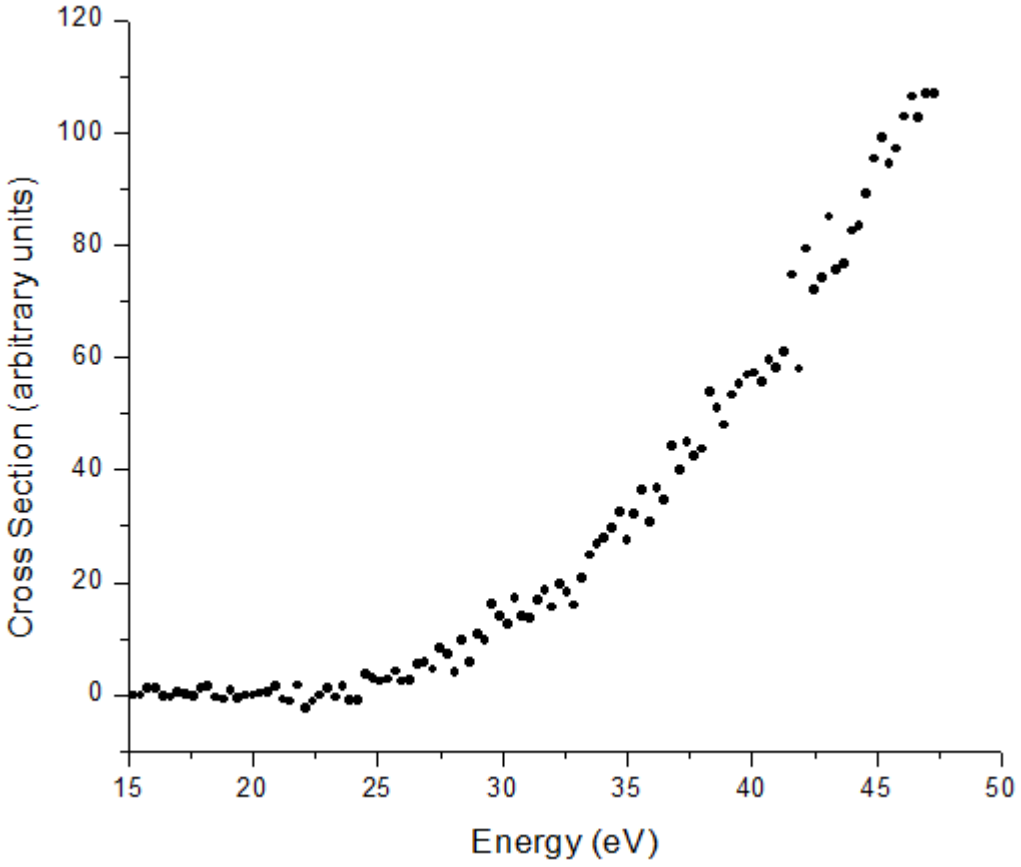

Figure 4.5: The emission cross section of Lyman-α transition as a function of electron-impact energy near threshold. The electron impact energy ranged from 15 eV to 50 eV.

However, stripping a H atom from any of the C or N sites of the molecule is certainly not the only way to acquire a H atom. Mass spectrometry work [15][33][29] has shown that H atoms are often produced by more complicated dissociation channels of the molecule. For

example, H can be produced from such a dissociation channel:

$$e + \mathrm{T} \rightarrow \mathrm{C_4H_4NO^+} + \mathrm{HNCO} + \mathrm{H} + e' + e'' \tag{4.6}$$

Indeed, work by van der Burgt et al.[15] has shown that the appearance of heavy fragments often accompanies with it one or more H atoms. These fragments have been identified in their work to have the following masses: 13, 14, 15 u; 26, 27, 28 u; 37, 38, 39, 40 u; 51, 52, 53, 54, 55 u; and 82 and 83 u. Some of these fragments are a part of the most significant features in thymine's mass spectrum [31], and so they should be expected to significantly contribute to the H signal observed. Dissociation channels that involve the appearance of these heavy fragments alongside the appearance of H atoms can account for the "late" onset of the Lyman-α relative cross section, with respect to the minimum energy expected to observe the transition; the appearance energy of the 82 u fragment, $\mathrm{C_4H_4NO^+}$, has been measured to be 12.8 eV by van der Burgt [15] and 13.2 eV by Jochims [33]. With the 10.2 eV required to promote ground state H to its 2p state, the appearance energy that should be expected to observe signal from H dissociated from this process is 23.0 eV to 23.4 eV, which is in agreement with our threshold measurement. However, the 54 u fragment was measured to have the same appearance energy as the 82 u fragment, which implies that discerning a dissociation process that results in a 82 u fragment or a 54 u fragment from the excitation function in Figure 4.5 is ambiguous. As mentioned by van der Burgt [15], despite a CO worth of mass difference between the 82 u and 54 u fragments, 54 u is not likely to be formed by CO loss from 82 u, though this does not rule out mass fragment 83 u being formed and then losing CO and H.

The 28 u mass fragment, which is expected to belong to a fragmentation process that involves H loss, would be expected at about 23.8 eV according to van der Burgt [15], which can partially contribute to the measured onset at 23.0 eV. Imhoff [31] has identified these fragments as $\mathrm{CO^+}$ or $\mathrm{HNCH^+}$, and accordingly it is the most intense feature in their mass

spectrum. It would be likewise difficult to separate a process resulting in 28 u from a process that results in 82 u or 54 u.

It is also suggested that the appearance energy of the 55 u fragment, identified as $HNC_3H_4^+$ by Imhoff [31] and also responsible for the production of H atoms, is 10.3 eV, meaning that some process beginning at least at 20.5 eV could potentially be seen. Since this is the the second most intense feature in the mass spectrum by Imhoff [31], it possibly contributes to the observed thresholds as in Figure 4.5.

The 39 u mass fragment is expected at about 24.6 eV according to van der Burgt [15], and identified by Imhoff [31] as $C_3H_3^+$. The associated H fragment could begin contributing to the signal in Figure 4.5 at about 25 eV, but this fragment does not appear to be very intense based on Imhoff's mass spectrum.

Schneider et al. [34] have studied the photodissociation of thymine in which photons of minimum energy of 4.59 eV were used to determine dissociation dynamics of thymine where ionic fragmentation is not involved. They had suggested a two photon process following the excitation of thymine to a $\pi\pi^*$ state; decay on a femtosecond timescale to a long-lived dark state follows, giving the opportunity for a second photon to be absorbed. It is suggested that the excited state resulting from the second absorption of a photon decays to the electronic ground state followed by a statistical dissociation of a H atom. The occurrence of a process like this implies a minimum of 9.18 eV. Detecting Lyman-α from a fragmentation that involves a similar process would require a minimum of 19.38 eV, well below our observed threshold.

It should also be noted that at about 33 eV the relative emission cross section begins to rise sharply, which suggests that multiple channels contribute to the detection of H fragments, however, given the work here it is not possible to quantify these channels; similar behaviour was observed in the ionization channels by van der Burgt [15].

4.4 Conclusions

Spectral measurements from 80 nm to 140 nm revealed evidence for fragmentation of hydrogen following 100 eV electron impact. Spectral features from other atomic fragments were not observed. Additionally, excitation studies indicated that a simple dissociation process where an excited hydrogen atom is stripped from any of its bonds, with no other fragments, does not significantly contribute to Lyman-α production. Instead it appears that H dissociation yielding Lyman-α radiation more likely occurs alongside the appearance of molecular fragments— including those of which that make up some of the most significant features in thymine's mass spectrum. Some fragmentation pathways that may be responsible for the appearance of Lyman-α have been discussed, but in some cases, the fragmentation pathways were not distinct due to these pathways possessing coincident threshold energies, or, the dominance of any one fragmentation pathway over another could not be thoroughly described. The shape of the excitation function for Lyman-α, as in Figure 4.3, indicated that optically allowed processes are significant, suggesting that the production of excited hydrogen fragments following the fragmentation of the parent molecule occurs as part of an initial ionizing collision.

Chapter 5

Electron Impact Studies on Adenine

5.1 Overview

Adenine was the second molecule studied in this work. Figure 5.1 is a diagram of the adenine molecule, which consists of a hexagonal ring attached to a pentagonal ring. There are two N atoms on each ring. On the larger ring there is a NH_2 branch and one H attached to the C2 site. On the smaller ring a lone H atom is attached to the N9 site, and another H is attached to the C8 site.

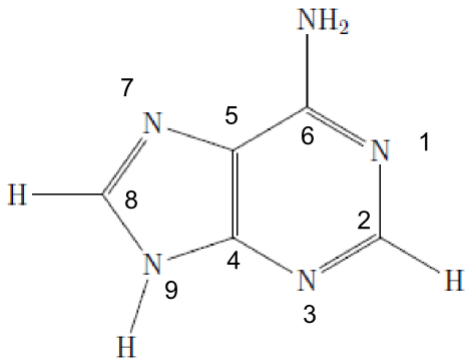

Figure 5.1: The molecular geometry of adenine.

Just as with thymine, adenine purchased from Sigma-Aldrich was loaded into the oven. The oven's body was heated to over 180 °C in order to sublimate the adenine and make a gas that could be intercepted by an electron beam. The stem settled at a temperature 40

°C higher than the body, which prevented adenine clogging through the capillary opening of the oven. Studies have been performed on adenine with similar temperatures [43][12]. The stem's temperature, despite being significantly hotter than the oven, was not expected to cause any thermal dissociation as the sublimated adenine should be heated mainly by the oven alone.

Similarly to thymine, photoemission spectra of adenine were taken over a wavelength range of 90 nm to 140 nm with a fixed electron energy beam of 100 eV. Additionally, the relative cross sections of the Lyman-alpha (121.6 nm) and Lyman-beta (102.6 nm) features were taken from 0-300 eV, for Lyman-alpha's case, and 0-400 eV, for Lyman-beta's case.

During spectrum measurement runs, the electron gun was kept constant at 50 μA. The behaviour of the current of the electron gun as it changed with energy was also monitored so that the relative cross sections of the spectral features could be corrected for changes in current. The energy resolution of the electron beam was about 1 eV at full-width half maximum, just as with thymine. Photon fluxes were assumed to be unpolarized due to the size of molecule complexity. As there was no capability to measure the pressure of the adenine beam, the absolute cross section could not be measured as in Equation 2.62.

5.2 Photoemission Spectra

Figure 5.2 displays the photoemission spectra of adenine taken from 90 nm to 140 nm with a fixed electron beam energy of 100 eV. The data has been corrected for the variation in detection probability across this wavelength region. Possible non-hydrogen atomic features that could have been measured from the dissociation of adenine are listed in Table 5.1, namely the most intense C or N features in this wavelength range. Similar to thymine, only the H Lyman series was detected.

All the H belong to the perimeter of the molecule while all the C and N make up the main ring structures. A single H fragment, with no other fragments, requires the breaking

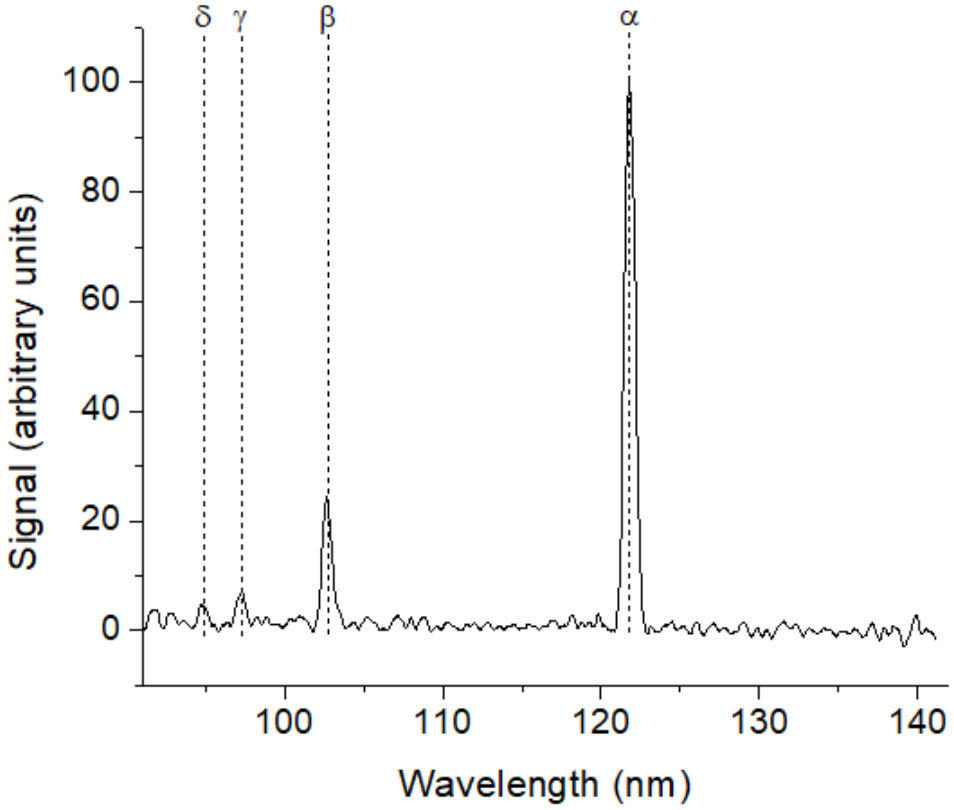

Figure 5.2: Adenine emission spectrum measured at constant electron impact energy of 100 eV with 0.2 mm slit width. The data have been corrected to take account of the spectral response of the detection system.

of a N-H bond or a C-H bond. Of the N-H bonds, one of the two N-H bonds off of the $C6$ must be broken, or the N-H bond on the smaller ring must be broken. Extracting a single C or N fragment should be significantly more difficult than extracting a H fragment due to the fact that, with the exception of the N in the NH_2, all the N or C are endocyclic.

Atomic fragment	Wavelength (nm)
C I	126.6
C I	127.8
C I	136.4
N I	120.4
N I	125.3

Table 5.1: Relevant non-hydrogen atomic features that could be observed from adenine. Taken from NIST.[1]

The fragmentation channels of adenine are dominated by molecular fragments that accompany atomic fragments. Comparison with electron mass spectrometry work by Minaev et al. [2] at 95 eV indicates that C^+ and N^+ ions contribute less than 1% to the entire mass spectrum, whereas H fragments can accompany some of the most intense features in the mass spectrum; these processes will be discussed later.

Feature	Wavelength (nm)	Transition	Relative Cross Section
α	121.6	H[2p-1s]	1.00
β	102.6	H[3p-1s]	0.23 ± 0.01
γ	97.3	H[4p-1s]	0.08 ± 0.01
δ	94.9	H[5p-1s]	0.05 ± 0.01
...	...	...	...
Lyman limit	91.2	H[∞p-1s]	N/A

Table 5.2: Features present in adenine emission spectrum.

Table 5.2 lists the features identified in the adenine photoemission spectra of Figure 5.2. Only the H Lyman series is present. Lyman-α is the dominant feature of the spectrum, followed by Lyman-β, Lyman-γ, and Lyman-δ. The rest of the Lyman series is present in the spectrum and terminates at the Lyman limit at 91.2 nm. As pressure could not be measured to determine an absolute cross section, relative cross sections are instead provided for β, γ, and δ in Table 5.2. The features present in the spectrum of Figure 5.2 were fitted with Gaussians, as discussed in Appendix E, and the areas of each fit were measured relative to Lyman-α. Of interest is the α:β intensity ratio of 1.00:0.23, which is higher than the measured 1.00:0.16 value determined for thymine.

Background studies performed with a cold oven revealed a molecular nitrogen contamination in the system as with thymine. This signal has been subtracted from the data.

5.3 Excitation Function Studies

As with thymine, the Lyman-α feature was chosen to measure its relative cross section as it varies with energy. Pressure could not be monitored along with the photon flux of the H radiation, and so these excitation functions are not provided in absolute terms. Figure 5.3 displays the total excitation function measured with the spectrometer fixed on Lyman-α radiation measured from 0 eV to 300 eV. The cross section has a broad peak at about 200 eV, which is located approximately 40 eV more than that of the peak for the total Lyman-α excitation of thymine seen in Figure 4.3. The overall shape seems to suggest that spin and optically allowed processes are dominant as the excitation function seems to decrease from the maximum as $\ln E/E$, a consequence from the Bethe-Born approximation discussed in Chapter 2.3. However, the energy range does not extend far enough to obtain a linear fit that properly tests the Bethe-Born approximation.

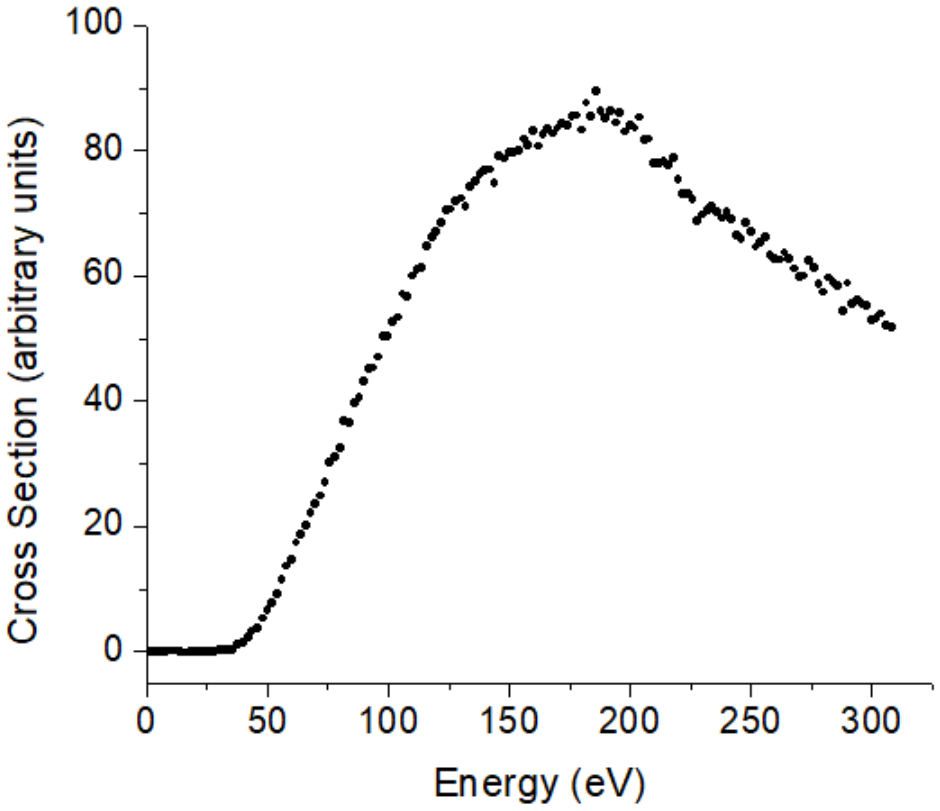

Figure 5.3: Lyman-α excitation function from 0 eV to 350 eV.

An excitation function with a smaller range, measured from 0 eV to 50 eV, to determine near-threshold behaviour is shown in Figure 5.4 where the onset appears rather late at 24 ± 1 eV followed by a more dominant process occurring at about 37 eV. These thresholds were determined by performing linear fits in the threshold region. This can be compared to the measured onset threshold energy for Lyman-α of 23.0 eV in Figure 4.5. Discussion of the Lyman-α threshold processes is given later in this work.

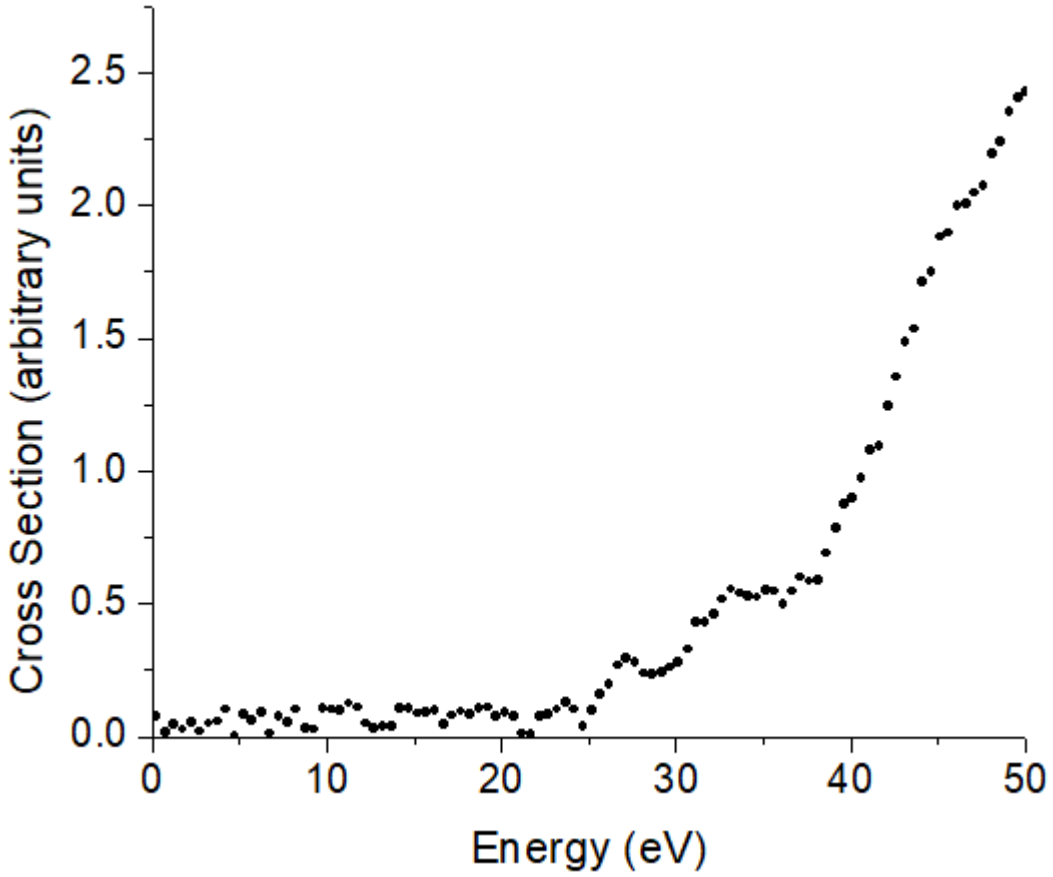

Figure 5.4: Lyman-α excitation function near threshold.

Excitation studies were also performed on Lyman-β, as can be seen in Figure 5.5, which shows the total excitation function for this transition.

The cross section rises to a broad maximum around 175 eV and falls off slowly with higher energies. As with thymine, the cross section is broadly unstructured for energies beyond the near-threshold region (50 eV or more). The energy range of this study does not extend

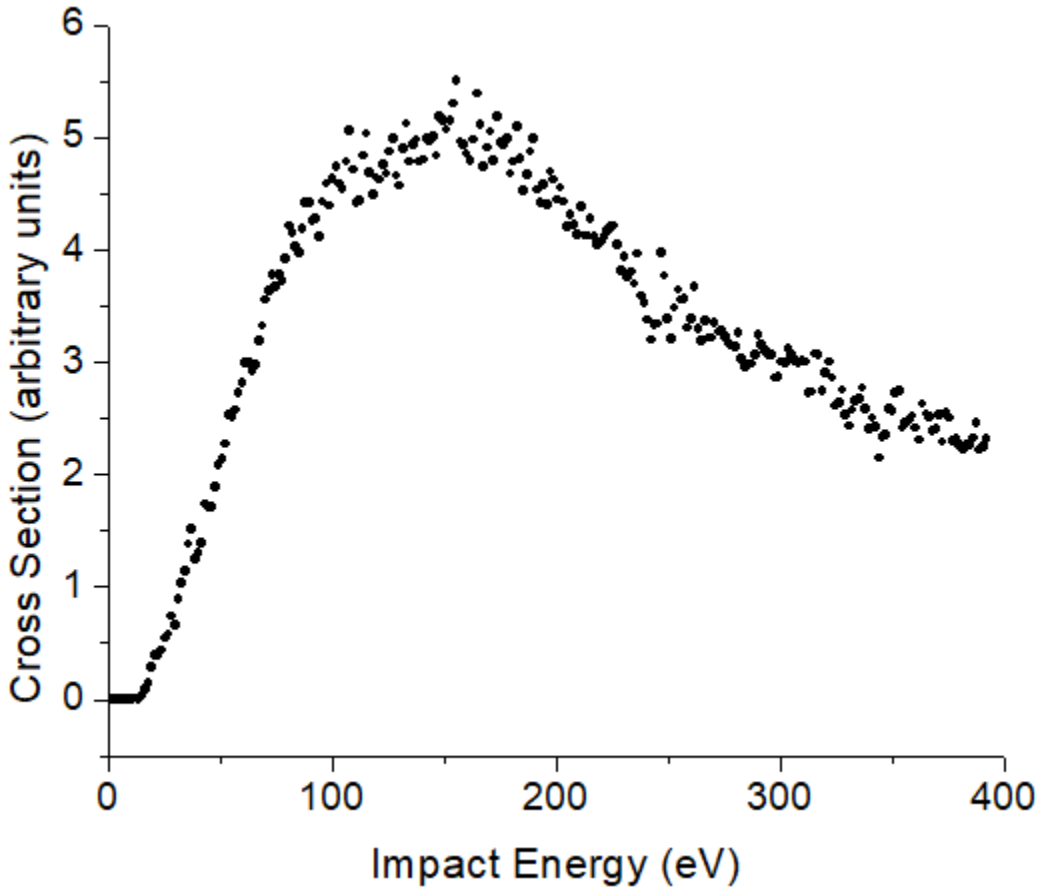

Figure 5.5: Lyman-β excitation function measured from 0 eV to 400 eV.

far enough to make a proper conclusion from the Bethe-Born approximation, however, the decrease in the cross section following the maximum goes approximately as 1/E, suggesting that spin-allowed but dipole-forbidden processes are important.

The near-threshold behaviour of the excitation function is shown in Figure 5.6. The threshold for the excitation function for Lyman-β was measured using a linear fit in the region and found to be

$$E_t[H(102.6\text{ nm})] = 18.0 \pm 1.0\text{ eV} \tag{5.1}$$

As with thymine, this threshold was corrected by using a well-known threshold energy of a calibration gas, as discussed in Appendix D. Gas phase electron energy loss experiments performed by Dillon et al. [45] showed a broad unstructured peak at 5 eV. Additionally,

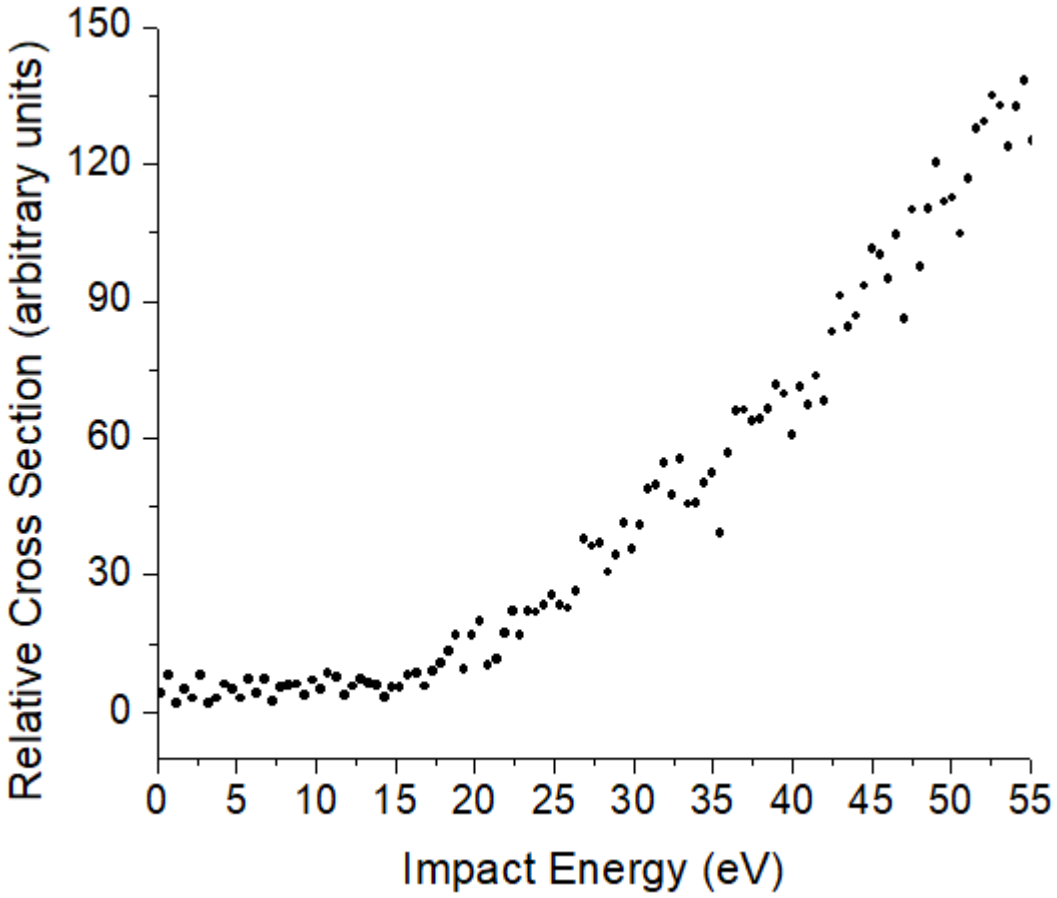

Figure 5.6: Lyman-β excitation function near threshold.

further experimental and theoretical work performed with respect to gas phase adenine and also on monolayers has shown that this broad feature at 5 eV does exist; this feature is indicative of a dissociation of the parent molecule. Hünig et al. [46] photolysed adenine with 243 nm (5 eV) photons and a REMPI process to determine the products of this dissociation, which were identified to be ground state H atoms. In the case for detecting Lyman-β radiation in this work, the H atoms from this dissociation process requires 12.2 eV for the emission of a photon from the H(3p) state to the H(1s) state. This would suggest a minimum appearance energy of 17.2 eV, which is in line with the 18.0 $\pm$ 1.0 eV threshold measurement made on the excitation function from Figure 5.6. This dissociation process

leads to the production of the 134 u mass fragment:

$$e + \mathrm{H_5C_5N_5} \rightarrow \mathrm{H_4C_5N_5} + \mathrm{H(3p)} + e' \tag{5.2}$$

Additional fragmentation processes are possible. Jochims et al. [33] have shown that the following process, an additional way to produce the 134 u mass fragment alongside ground state H has an appearance energy of 10 eV.

$$e + \mathrm{H_5C_5N_5} \rightarrow \mathrm{H_4C_5N_5^+} + \mathrm{H} + e' + e'' \tag{5.3}$$

A process like this with a dissociated H promoted to an np state could appear about 25 eV granted that the fragments possess some kinetic energy.

As with thymine, there are other fragmentation channels in which it is possible that excited H is produced along with some molecular fragment. Mass spectrometry work by Rice et al. [29], Minaev et al. [2], Jochims et al. [33] and others has made it possible to identify the major fragmentation pathways that occur for adenine. Minaev suggests four primary fragmentation routes for adenine, which are summarized in Table 5.3.

Route	Neutral Loss	Mass (u)	Charged Fragment Loss	Mass (u)	Broken Bonds
1	$C_4H_3N_4$	107	CH_2N^+	28	N1-C6 and C5-C6
2	$C_2H_3N_2$	55	$C_3H_2N_3{}^+$	80	C5-C6 and N3-C2
3	$C_4H_3N_4$	107	CH_2N^+	28	N7-C8 and N9-C4
4	HCN	27	$C_4H_4N_4{}^+$	108	N1-C6 and C2-N3

Table 5.3: Main primary fragmentation pathways for adenine as proposed by Minaev et al. [2].

What follows involves a discussion of these fragmentation pathways, which for some do not immediately lead to excited H production as was the case with thymine. However, it is possible that excited H is produced during the chains of dissociation, or at the end of these fragmentation pathways, such as in the most significant fragmentation pathway for excited adenine, which involves successive losses of HCN units. It is most likely initiated by way of

Route 4 in which a HCN unit is removed from the parent molecule to form the 108 u mass fragment.

$$C_5H_5N_5^+ \rightarrow C_4H_4N_4^+ + HCN \tag{5.4}$$

The most likely way for adenine to lose its first HCN unit is from the breaking of the N1-C6 and C2-N3 bonds. The ions produced from the dissociation are not stable and tend to shed off more fragments. Following the initial HCN loss by way of Route 4, the 108 u fragment can transfer one or two H to the N3 site, reconfiguring itself in one of two isomers depending on the number of H transferred. Following one H transfer, an additional HCN unit loss may occur to form the 81 u mass fragment.

$$C_4H_4N_4^+ \rightarrow C_3H_3N_3^+ + HCN \tag{5.5}$$

The 81 u mass fragment can then undergo successive HCN losses to form 54 u and 27 u fragments by the following processes.

$$C_3H_3N_3^+ \rightarrow C_2H_2N_2^+ + HCN \tag{5.6}$$

$$C_2H_2N_2^+ \rightarrow HCN^+ + HCN \tag{5.7}$$

If the 108 u fragment undergoes double H transfer and forms an alternative isomer, it will shed a NH_2CN unit in the following way to form the 66 u fragment.

$$C_4H_4N_4^+ \rightarrow NH_2CN + C_3H_2N_2^+ \tag{5.8}$$

The fragmentation pathways as explained above involve the most significant ways in which the parent molecule dissociates, however they do not produce H so alternative fragmentation channels must be assessed.

The 108 u mass fragment is a dominant fragment in the mass spectra, but alongside it

there is the 107 u and 106 u fragments. Sethi et al. [32] and Minaev et al. [2] suggest that 107 u and 106 u can be created from one or two H loss, respectively, from the 108 u fragment. However, from Routes 1 and 3 from Table 5.3 and Jochims et al. [33], the 107 u fragment can appear without the need for H loss from 108 u. The 106 u fragment appears in Minaev's work with the same relative intensity as the 107 u fragment in the mass spectrum, but does not appear in Rice et al. [29] or in van der Burgt et al. [12]. However, appearance energy measurements of mass fragments by van der Burgt does not contradict H loss as a possible dissociation process.

The 81 u fragment, formed from an initial HCN loss followed by one H transfer and then a second HCN loss, can lose H to form the 80 u fragment, which is present in Rice, Minaev, and van der Burgt. This H loss is suggested by Sethi et al. [32] and Minaev et al. [2], but an additional, alternative process is proposed by Minaev as indicated by Route 2 in Table 5.3. Jochims et al. [33] explains the appearance of this fragment by the formation of a charged 107 u fragment by the following process.

$$C_5H_5N_5^+ \rightarrow C_4H_3N_4^+ + H_2CN \tag{5.9}$$

The $C_4H_3N_4^+$ can lose one HCN unit to form $C_3H_2N_3^+$, an 80 u mass fragment without the need for H loss. However, as with the 107 u fragment, appearance energy measurement work performed by van der Burgt [12] permits H loss as a possible method for the appearance of the 80 u fragment.

The 54 u fragment, formed from a third successive HCN loss, has been suggested by Sethi et al. [32] and Minaev et al. [2] to lose one or two H for the appearances of the 53 u and 52 u fragments. Jochims et al. [33] explains the appearance of $C_2HN_2^+$, a fragment with mass of 53 u, by way of an initial H_2CN loss from adenine followed by two successive HCN losses, a fragmentation pathway that does not involve H loss. Appearance energy measurements of 54 u, 53 u, and 52 u by van der Burgt et al. [12] allow H loss to be a plausible way for such

fragments to be formed. The 52 u fragment does not appear to be measured in Jochims [33] nor its appearance energy by van der Burgt et al. [12], however it does appear in the mass spectra work of Minaev et al. [2] and Rice et al. [29]; additionally, the intensity of the 53 u fragment is higher than the 80 u fragment in the mass spectra, which suggests an 80 u to 53 u pathway by one HCN loss can be accompanied by H loss from 54 u for the production of 53 u.

The fragments with masses of 29 u, 28 u, 27 u, and 26 u are prominent in mass spectra work for adenine. The 29 u fragment has the elemental formula CH_3N^+ and is suggested by Jochims et al. [33] to be the NH_2CH^+ ion. The 28 u fragment, as formed by Route 3 in Table 5.3, is more intense than the 29 u fragment, and as its appearance energy is less than the appearance energy of the 29 u fragment, it is not expected that H is lost from 29 u to form 28 u. The 27 u fragment has the elemental formula HCN and, as discussed, has plentiful pathways to be formed without the need for any H loss. However, the appearance of the 26 u fragment, identified with the elemental formula as CN, could be formed from H loss from 27 u. A possible pathway that involves a mass fragment of 26 u with H production could involve the loss of HCN units and lead to H production excited to some np level.

$$H_5C_5N_5 + e \rightarrow x(HCN) + CN + H(np) + \text{ion fragments} + me' \tag{5.10}$$

(x = 0 to 4; m $\geq$ 1)

The appearance energy for the fragmentation processes described above are all within the 12-14 eV range [12][33][37]. With this known, and with the expectation that some more energy would be expected for the additional dissociation process that occurs in Equation 5.10 to yield excited H atoms, the appearance energy for Lyman-α or Lyman-β radiation for such dissociation events would be expected to be in the range of 25 to 35 eV. This may contribute to the near-threshold behaviour of the Lyman-α excitation function as seen in Figure 5.4.

It is worth mentioning again that the threshold for Lyman-α, seen in Figure 5.4, was

measured to be

$$E_t[H(121.6\text{ nm})] = 24.0 \pm 1.0\text{ eV} \tag{5.11}$$

This is a surprising result as this threshold is not 2 eV lower than the Lyman-β threshold, measured as 18 eV, but instead is significantly higher. It can also be seen in Figure 5.4 that after the initial onset, a more dominant process takes over at about 37 eV. This sort of behaviour contradicts the sort of process that happens in Equation 5.2, where a single excited H is stripped from the parent molecule; if this were happening, the threshold onset would begin at approximately 15.2 eV. This may be due to a fast radiationless transfer of energy from the excited parent molecule to a lower state, as discussed by Broo [47] and others [48][49]. Another consequence of this measurement is that the kind of dissocation as given in Equation 5.2 is not a two-step process in which the H atom is dissociated and then excited; if it were, excitation of the H(2p) or H(3p) states should occur with similar possibility. The contribution of the process as given in Equation 5.2 to the appearance of Lyman-β but not to Lyman-α may explain the higher α:β ratio for adenine, listed in Table 5.1, as compared to work done for thymine or in previous work done with pyrimidine [8].

5.4 Conclusions

Spectral measurements from 85 nm to 140 nm indicated evidence for the dissociation of excited H fragments from the parent molecule due to the presence of the Lyman series. The spectral features from other atomic fragments in the VUV range were not observed, as with thymine, indicating low probability for extracting excited C or N fragments. Excitation studies revealed that a simple dissociation process where hydrogen is stripped from the parent molecule does not likely yield Lyman-α hydrogen. However, this process is consistent with the measured threshold energy of Lyman-β, suggesting such a simple dissociation process can yield H(3p). The threshold measurements indicate some possible fragmentation pathways, but it was not possible to uniquely qualify them.

Chapter 6

Conclusion

The dissociative excitation of thymine and adenine has been studied in the VUV spectral range. Measurements of emission spectra were performed for thymine from 85 nm to 125 nm and for adenine from 90 nm to 140 nm. These studies revealed that the only significant products in this region from electron impact were H(np) atoms as indicated by the Lyman series present in the measurements. Additionally, the relative cross sections, α:β:γ, for both thymine and adenine were determined to be 1.00:0.16:0.08 and 1.00:0.23:0.08, respectively. In the case for thymine, no excited C, N, or O atomic fragments were observed. For adenine, neither C or N excited products were observed. This is consistent with dissociative ionization measurements that indicated non-hydrogen atomic ions make up a very small portion of the total ionization products.

Excitation functions were obtained for the H(2p$\rightarrow$1s) transition for thymine and on the H(2p$\rightarrow$1s) and H(3p$\rightarrow$1s) transitions for adenine. Threshold measurements on the H(2p$\rightarrow$1s) transition with thymine were consistent with ionization measurements where fragmentation pathways were studied, mainly that excited H atoms dissociate more likely as a product that comes along with molecular fragments rather than being singularly dissociated from the parent molecule. Threshold measurements for the studied H transitions with adenine unexpectedly showed a +6 eV discrepancy between Lyman-α and Lyman-β rather than a -2

eV difference, which may be due to a radiationless process where energy is rapidly transferred to a lower state as discussed by Broo and others [47]. This could be a possible reason for the higher α:β cross section ratio compared to the relative cross sections measured for thymine in this work and in pyrimidine work by Hein et al. [8]. Measurements performed on the Lyman-β excitation function indicates that near threshold, dissociation of H atoms most likely occurs by being singularly cleaved from the parent molecule. At energies of 25 eV or higher, H dissociation is dominated by processes with more complicated break-up channels. The fragmentation pathways for adenine [2] indicate that the parent molecule breaks up in many molecular pieces, especially in multiples of HCN units, and such ways of producing excited H may be less for adenine than for thymine.

The excitation function of the H(2p$\rightarrow$1s) transition for thymine was measured with a broad maximum at about 160 eV; at the highest energies it falls-off as approximately ln(E)/E, which suggests dipole-allowed processes are significant. Similarly, the excitation functions for the H(2p$\rightarrow$1s) and H(3p$\rightarrow$1s) transitions for adenine were measured; Lyman-α had a broad maximum about 200 eV while Lyman-β had a broad maximum about 175 eV. Both of these excitation functions seemed to go as 1/E at higher energies, suggesting the importance of spin-allowed but dipole-forbidden processes in this case.

In future investigations, atomic fragmentation of cytosine could be studied. One advantage of studying cytosine is that it is a liquid at room temperature like pyrimidine. In the work by Hein et al. for pyrimidine [8], which involved a different configuration of the experimental apparatus, it was possible to measure the cross section data and calibrate it in absolute terms due to pyrimidine's liquid property. Pyrimidine was introduced into the chamber in a different way from the oven; it was delivered from a stainless steel tube via a gas line into a delivery tube that formed a beam of pyrimidine gas directly above the electron beam. In the previous set-up for the chamber, not only could the delivery tube pressure be monitored, but another calibration gas could be passed through the delivery tube, ensuring ease of replicating similar experimental conditions for the collision chamber, which is nec-

essary to determine the absolute cross section, as discussed in the end of Chapter 2.4. In past work, the absolute cross sections for pyrimidine in the VUV range were determined by measuring them relative to the well-known H_2 cross sections. A similar experimental scheme can be performed with cytosine to obtain measurements of absolute cross sections in the VUV wavelength range, but will require the experimental apparatus to be reverted to the previous configuration involving the delivery tube system.

A similar procedure can be done to determine absolute cross sections for thymine and adenine, but this will require a major re-design of the biomolecule oven. The oven will have to be modified to allow a calibration gas to pass through its capillary tube. Alternatively, an entirely new oven may have to be designed to make this possible. Additionally, the apparatus will have to be adapted so that the vapour pressure of the sublimated beam can be measured during measurements. Once this is done, absolute cross section measurements may be performed on the Lyman series for thymine and adenine.

Finally, an additional target for future electron dissociation studies could be guanine, which is a solid at room temperature like thymine and adenine. At the least, the studies done in this work could be performed on guanine to obtain information on the atomic fragmentation processes. Additionally, this will enable us to observe the possible dissociation pathways near threshold. If the experimental apparatus is reconfigured to allow absolute cross section measurements for the targets that require sublimation, then absolute cross section measurements in the VUV wavelength range for guanine may be performed. It will be worthwhile to extend the work done here from thymine and adenine to guanine and cytosine as the latter two molecules make up the remaining two main nucleobases of DNA.

Bibliography

[1] A. Kramida, Yu. Ralchenko, J. Reader, and and NIST ASD Team. NIST Atomic Spectra Database (ver. 5.5.6), [Online]. Available: https://physics.nist.gov/asd [2017, April 9]. National Institute of Standards and Technology, Gaithersburg, MD., 2018.

[2] B. F. Minaev, M. I. Shafranyosh, Yu. Yu Svida, M. I. Sukhoviya, I. I. Shafranyosh, G. V. Baryshnikov, and V. A. Minaeva. Fragmentation of the adenine and guanine molecules induced by electron collisions. *The Journal of Chemical Physics*, 140(17):175101, 2014.

[3] A. K. Abdellatif. *Electron impact excitation studies of unstable atomic species*. PhD thesis, University of Windsor, 2003.

[4] D. Ferro, L. Bencivenni, R. Teghil, and R. Mastromarino. Vapour pressures and sublimation enthalpies of thymine and cytosine. *Thermochimica Acta*, 42(1):75 – 83, 1980.

[5] W. Zielenkiewicz. Enthalpies of Sublimation and Vapor Pressures of Adenine, 1-Methyladenine, 2-Methyladenine, 3-Methyladenine, and 8-Methyladenine. *Journal of Chemical & Engineering Data*, 45(4):626–629, 2000.

[6] S. J. Brotton, E. Vyskocil, W. Kedzierski, and J. W. McConkey. Dissociative excitation of H_2S by electron impact. *Phys. Rev. A*, 79:042709, 2009.

[7] S. J. Brotton and J. W. McConkey. Electron-impact dissociative excitation of S_2. *Journal of Physics B: Atomic, Molecular and Optical Physics*, 44(21):215202, 2011.

[8] J. D. Hein, H. Al-Khazraji, C. J. Tiessen, D. Lukic, J. A. Trocchi, and J. W. McConkey. Excited atomic fragments following electron dissociation of pyrimidine. *Journal of Physics B: Atomic, Molecular and Optical Physics*, 46(4):045202, 2013.

[9] P. Możejko and L. Sanche. Cross section calculations for electron scattering from DNA and RNA bases. *Radiation and Environmental Biophysics*, 2003.

[10] S. D. McCulloch and T. A. Kunkel. The fidelity of DNA synthesis by eukaryotic replicative and translesion synthesis polymerases. *Cell Res.*, 18(1), 2008.

[11] J. H. Hoeijmakers. DNA damage, aging, and cancer. *N. Engl. J. Med.*, 361(15):1475–85, 2009.

[12] P. J. M. van der Burgt, S. Finnegan, and S. Eden. Electron impact fragmentation of adenine: partial ionization cross sections for positive fragments. *The European Physical Journal D*, 69(7):173, 2015.

[13] Eric J. Hall. *Radiobiology for the Radiobiologist*. Lippincqtt Williams & Wilkins, 2000.

[14] B. Boudaıffa, P. Cloutier, D. Hunting, M. A. Huels, and L. Sanche. Resonant Formation of DNA Strand Breaks by Low-Energy (3 to 20 ev) Electrons. *Science*, 287(5458):1658–1660, 2000.

[15] P. J. M. van der Burgt, F. Mahon, G. Barrett, and M. L. Gradziel. Electron impact fragmentation of thymine: partial ionization cross sections for positive fragments. *The European Physical Journal D*, 2014.

[16] H. Hotop, M.-W. Ruf, M. Allan, and I.I. Fabrikant. Resonance and Threshold Phenomena in Low-Energy Electron Collisions with Molecules and Clusters. *Advances In Atomic, Molecular, and Optical Physics*, 49:85 – 216, 2003.

[17] R. Balog, J. Langer, S. Gohlke, M. Stano, H. Abdoul-Carime, and E. Illenberger. Low energy electron driven reactions in free and bound molecules: from unimolecular pro-

cesses in the gas phase to complex reactions in a condensed environment. *International Journal of Mass Spectrometry*, 233(1):267 – 291, 2004.

[18] L. Sanche. Low energy electron-driven damage in biomolecules. *The European Physical Journal D - Atomic, Molecular, Optical and Plasma Physics*, 35(2):367–390, 2005.

[19] I. Baccarelli, I. Bald, F. A. Gianturco, E. Illenberger, and J. Kopyra. Electron-induced damage of DNA and its components: Experiments and theoretical models. *Physics Reports*, 508(1):1 – 44, 2011.

[20] C. J. Colyer, S. M. Bellm, F. Blanco, G. García, and B. Lohmann. Elastic electron scattering from the DNA bases cytosine and thymine. *Phys. Rev. A*, 84:042707, 2011.

[21] R Abouaf, J. Pommier, and H. Dunet. Electronic and vibrational excitation in gas phase thymine and 5-bromouracil by electron impact. *Chemical Physics Letters*, 381(3):486 – 494, 2003.

[22] I. V. Chernyshova, E. J. Kontros, P. P. Markush, and O. B. Shpenik. Excitation of lowest electronic states of thymine by slow electrons. *Optics and Spectroscopy*, 115(5):645–650, 2013.

[23] C. Winstead, V. McKoy, and S. dAlmeida Sanchez. Interaction of low-energy electrons with the pyrimidine bases and nucleosides of DNA. *The Journal of Chemical Physics*, 127(8):085105, 2007.

[24] A. Dora, L. Bryjko, T. van Mourik, and J. Tennyson. R-matrix study of elastic and inelastic electron collisions with cytosine and thymine. *Journal of Physics B: Atomic, Molecular and Optical Physics*, 45(17):175203, 2012.

[25] I. I. Shafranyosh and M. I. Sukhoviya. Inelastic collisions of the uracil molecules with electrons. *The Journal of Chemical Physics*, 137(18):184303, 2012.

[26] I. I. Shafranyosh, V. V. Stetsovich, N. N. Chavarga, and M. I. Sukhoviya. Electron impact excitation of luminescence of uracil. *Optics and Spectroscopy*, 112(2):155–158, 2012.

[27] O. B. Shpenik, N. M. Erdevdy, V. V. Zvenighorodsky, and L. G. Romanova. Luminescence of cytosine vapor excited by slow electrons. *Journal of Applied Spectroscopy*, 80(1):43–46, 2013.

[28] O. B. Shpenik, M. M. Erdevdi, V. V. Zvenigorodsky, and A. A. Borovik. Electron Impact Excitation of Gas-Phase Adenine Molecule. *Journal of Physics: Conference Series*, 388(5):052047, 2012.

[29] J. M. Rice and G. O. Dudek. Mass spectra of nucleic acid derivatives. II. Guanine, adenine, and related compounds. *Journal of the American Chemical Society*, 89(11):2719–2725, 1967. PMID: 6043801.

[30] J. Ulrich, R. Teoule, R. Massot, and A. Cornu. Etude de la fragmentation de derives de L'uracile et de la thymine par Spectrometrie de masse. *Organic Mass Spectrometry*, 2(12):1183–1199, 1969.

[31] M. Imhoff, Z. Deng, and M. A. Huels. Identification of ion fragments produced from thymine and deuterated thymine by low energy ion impact in films and electron impact in the gas phase. *International Journal of Mass Spectrometry*, 245:68–77, 2005.

[32] S. Sethi, S. P. Gupta, E. E. Jenkins, C. W. Whitehead, Leroy B. Townsend, and James A. McCloskey. Mass spectrometry of nucleic acid constituents. Electron ionization spectra of selectively labeled adenines. *Journal of the American Chemical Society*, 104(12):3349–3353, 1982.

[33] H.W. Jochims, M. Schwell, and H. Baumg˙ Photoion mass spectrometry of adenine, thymine and uracil in the 6—22 eV photon energy range. *Chemical Physics*, 314(1):263 – 282, 2005.

[34] M. Schneider, R. Maksimenka, F. J. Buback, T. Kitsopoulos, L. R. Lago, and I. Fischer. Photodissociation of thymine. *Phys. Chem. Chem. Phys.*, 8:3017–3021, 2006.

[35] S. Li, H. Guo, L. Zhang, and F. Qi. Dissociation Pathway Analysis of Thymine under Low Energy VUV Photon Excitation. *Chinese Journal of Chemical Physics*, 24(3):275–283, 2011.

[36] M. M. Dawley, K. Tanzer, W. A. Cantrell, P. Plattner, N. R. Brinkmann, P. Scheier, S. Denifl, and S. Ptasiska. Electron ionization of the nucleobases adenine and hypoxanthine near the threshold: a combined experimental and theoretical study. *Phys. Chem. Chem. Phys.*, 16:25039–25053, 2014.

[37] S. Pilling, A. F. Lago, L. H. Coutinho, R. B. de Castilho, G. G. B. de Souza, and A. N. de Brito. Dissociative photoionization of adenine following valence excitation. *Rapid Communications in Mass Spectrometry*, 21(22):3646–3652, 2007.

[38] M. Inokuti, Y. Itikawa, and J. E. Turner. Addenda: Inelastic collisions of fast charged particles with atoms and molecules—The Bethe theory revisited. *Rev. Mod. Phys.*, 50:23–35, 1978.

[39] H. Bethe. Zur Theorie des Durchgangs schneller Korpuskularstrahlen durch Materie. *Annalen der Physik*, 397(3):325–400, 1930.

[40] U. Fano. Ionizing Collisions of Very Fast Particles and the Dipole Strength of Optical Transitions. *Phys. Rev.*, 95:1198–1200, 1954.

[41] D.W.O. Heddle and R.G.W. Keesing. Measurements of Electron Excitation Functions. *Advances in Atomic and Molecular Physics*, 4:267 – 298, 1968.

[42] P. N. Clout and D. W. O. Heddle. Elimination of instrumental polarization from polarization measurements. *Journal of Physics E: Scientific Instruments*, 2(11):929, 1969.

[43] M. Rahman and E. Krishnakumar. Electron ionization of DNA bases. *The Journal of Chemical Physics*, 144:161102, 2016.

[44] J.W. McConkey, C.P. Malone, P.V. Johnson, C. Winstead, V. McKoy, and I. Kanik. Electron impact dissociation of oxygen-containing molecules—A critical review. *Physics Reports*, 466(1):1 – 103, 2008.

[45] M. A. Dillon, H. Tanaka, and D. Spence. The Electronic Spectrum of Adenine by Electron Impact Methods. *Radiation Research*, 117(1):1–7, 1989.

[46] I. Hünig, C. Plützer, K. A. Seefeld, D Löwenich, M Nispel, and K Kleinermanns. Photostability of Isolated and Paired Nucleobases: N-H Dissociation of Adenine and Hydrogen Transfer in its Base Pairs Examined by Laser Spectroscopy. *ChemPhysChem*, 5(9):1427–1431, 2004.

[47] A. Broo. A Theoretical Investigation of the Physical Reason for the Very Different Luminescence Properties of the Two Isomers Adenine and 2-Aminopurine. *The Journal of Physical Chemistry A*, 102(3):526–531, 1998.

[48] M. G. D. Nix, A. L. Devine, B. Cronin, and M. N. R. Ashfold. Ultraviolet photolysis of adenine: Dissociation via the $^1\pi\sigma^*1^*$ state. *The Journal of Chemical Physics*, 126(12):124312, 2007.

[49] A. L. Sobolewski, W. Domcke, C. Dedonder-Lardeux, and C. Jouvet. Excited-state hydrogen detachment and hydrogen transfer driven by repulsive $^1\pi\sigma^*$ states: A new paradigm for nonradiative decay in aromatic biomolecules. *Phys. Chem. Chem. Phys.*, 4:1093–1100, 2002.

[50] E. McDaniel. *Atomic collisions: Electron and Photon Projectiles*. Wiley, 1989.

[51] J. Tabet, S. Eden, S. Feil, H. Abdoul-Carime, B. Farizon, M. Farizon, S. Ouaskit, and T.D. Mrk. Absolute molecular flux and angular distribution measurements to charac-

terize DNA/RNA vapor jets. *Nuclear Instruments and Methods in Physics Research Section B: Beam Interactions with Materials and Atoms*, 268(15):2458 – 2466, 2010.

[52] K. Malek and M. Coppens. Knudsen self- and Fickian diffusion in rough nanoporous media. *The Journal of Chemical Physics*, 119(5):2801–2811, 2003.

[53] H. D. Morgan and J. E. Mentall. EUV studies of N_2 and O_2 produced by low energy electron impact. *The Journal of Chemical Physics*, 78(4):1747–1757, 1983.

Appendix A

Scientific Constants

Quantity	Symbol	Value	Units
Electron volt	eV	1.602 176 565(35) $\times 10^{-19}$	J
Boltzmann's constant	k_B	1.380 648 8(13) $\times$ 10^{-23}	J/K
Elementary charge	e	1.602 176 565(35)$\times 10^{-19}$	C
Planck's constant	h	6.626 069 57(29)$\times 10^{-34}$	Js
Reduced Planck's constant	$\hbar$	1.054 571 726(47)$\times 10^{-34}$	Js
Bohr radius	a_0	0.529 177 210 92(17)$\times 10^{-10}$	m
Electron mass	m_e	9.109 382 91(40)$\times 10^{-31}$	kg
Ideal Gas Constant	R	8.3144598(48)	J/(mol K)
Torrent	Torr	133.322	Pa
Molar Mass of Thymine	M_T	126.1133	g/mol
Molar Mass of Adenine	M_A	135.13	g/mol
Rydberg constant	R_∞	10 973 731.568 508 (65)	m^{-1}

Appendix B

Jet Flow Estimations of Thymine and Adenine

In this experiment, thymine and adenine were loaded into an oven with a capillary tube outfitted with an array of 3 by 5 effusion holes, each with a radius of 0.035 inches. The tube was heated to at least 150 °C so that condensation within the tube was avoided. Thermal collisions between the molecules is considered here in order to determine an estimate for the type of vapour flow that occurs from the oven. Vapour pressures are also estimated.

Firstly, by considering a gas of spherical particles that interact with each other only by elastic collisions, the distributions of their velocities, v, can be described by the Maxwell-Boltzmann distribution [50].

$$f(v)dv = \left(\frac{m}{2\pi k_B T}\right)^{3/2} 4\pi v^2 \exp\left(\frac{-mv^2}{2k_B T}\right) dv \tag{B.1}$$

The mass of the particle that makes up the gas is m, which is held at temperature T. k_B is Boltzmann's constant. From here, the mean speed $\langle v \rangle$, most probable speed v_p, and root-mean-square speed v_{rms} can be calculated. For instance, v_p can be determined by taking the derivative of Equation 1.1 and solving for a solution. In that case, one obtains the following

expression for the most probable speed.

$$v_p = \sqrt{\frac{2k_BT}{m}} \tag{B.2}$$

The mean velocity $\langle v \rangle$ can be determined by calculating the expectation value of the entire distribution.

$$\langle v \rangle = \int_0^\infty v f(v) dv = \sqrt{\frac{8k_BT}{\pi m}} \tag{B.3}$$

It easily follows that the mean velocity is proportional to the most probable speed.

$$\langle v \rangle = \frac{2}{\sqrt{\pi}} v_p \tag{B.4}$$

Next, one may want to consider the mean free path of these particles, which is the average distance a particle of this gas will travel without colliding into the other particles, and can be defined using the mean velocity. We can formulate the mean free path by taking the distance travelled by the particle and dividing it by the volume of interaction where the particle may find a target and also by the number of molecules per unit volume. To do so, we will want to consider the average relative velocity of the targets, $\langle v_{rel} \rangle$. It can be shown that this quantity can be written in the following way.

$$\langle v_{rel} \rangle = \sqrt{2} \langle v \rangle \tag{B.5}$$

We now wish to return to the mean free path. A particle of the ideal gas travels at $\langle v \rangle$ and in time t covers a distance of $\langle v \rangle t$ and has an effective collision cross section of $\pi\sigma^2$. A random target with $\langle v_{rel} \rangle$ will, in the same time, cover a distance of $\langle v_{rel} \rangle t = \sqrt{2}\langle v \rangle t$. Then the volume of interaction is $\pi\sigma^2\sqrt{2}\langle v \rangle t$. Then, with the number of molecules per unit volume, n_V, the mean free path, λ, can be expressed in this way.

$$\lambda = \frac{\langle v \rangle t}{\pi\sigma^2\sqrt{2}\langle v \rangle t n_V} = \frac{1}{\sqrt{2}\pi\sigma^2 n_V} \tag{B.6}$$

The ideal gas law allows the above equation to be written in a form that contains the vapour pressure, P, and temperature of the gas as according to this law:

$$n_V = \frac{N}{V} = \frac{P}{k_B T} \tag{B.7}$$

Then, the mean free path for a hard spherical particle that makes up an ideal gas can be rewritten in this way.

$$\lambda = \frac{k_B T}{\sqrt{2}\pi\sigma^2 P} \tag{B.8}$$

Unfortunately in the work done, we could not measure the vapour pressure of the sublimated target as it left the capillary tube in the oven; only pressures of a swarm gas distribution in which the entire chamber is filled with a target could be measured. However, a rough estimation was made to determine the vapour pressure. However, a few acknowledgements must be made: thymine and adenine are clearly not spherical, and the oven is not a closed system. The experiment is performed in vacuum at approximately 3×10^{-7} Torr and any gas in the system is continuously pumped out, and the sublimated biomolecule targets are always being emitted from the oven.

Ferro et al [4] have done work to measure the vapour pressures of thymine and cytosine. Figure B.1 features a plot that uses the Clausius-Clapeyron equation they measured to observe the vapour pressure as a function of temperature. Additionally, Zielenkiewicz [5] had measured enthalpies of sublimation for adenine and its methyl derivatives, and the data measured there were used to create the vapour pressure plots shown in Figure B.1.

Electron impact studies on these biomolecules were only performed after a steady-state oven temperature was achieved. A key goal was to use as low a temperature to sublimate the molecule as possible in order to avoid thermal decomposition and to reduce the vapour pressure to avoid viscous flow of the sublimated biomolecules and also so that all of sample target was not completely expelled from the oven too quickly. However, pressures could not

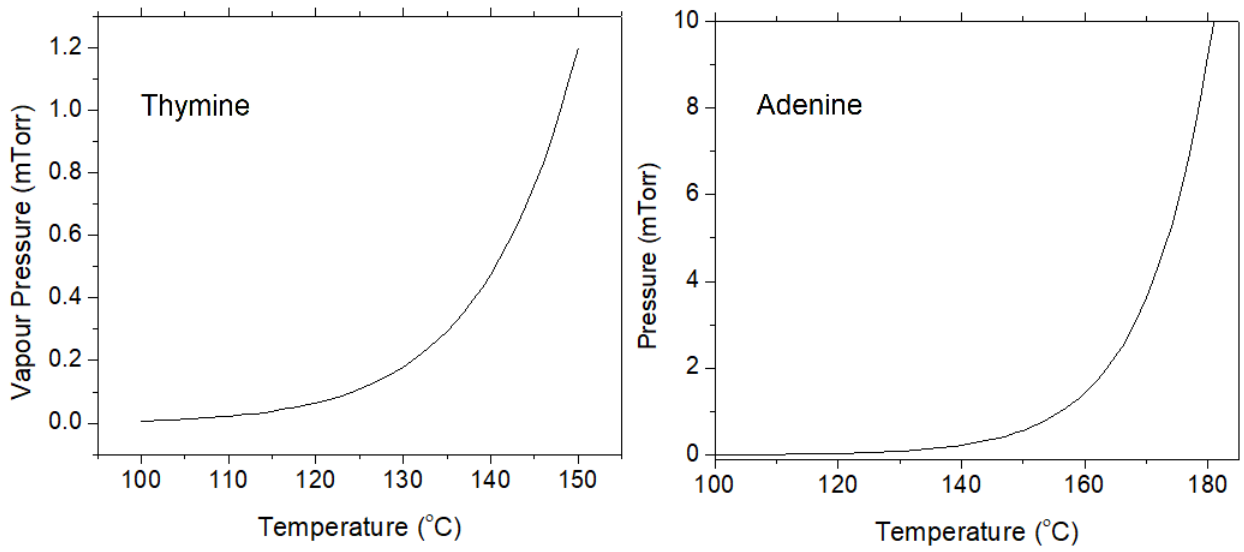

Figure B.1: Vapour pressure plots against temperature. The thymine plot on the left was done with [4]. The adenine plot on the right was done with [5].

be made arbitrarily low as this would reduce photon counts from electron impact measurements and require larger data sets in order to obtain usable statistics.

During electron impact measurements for thymine, the oven body was maintained at 150 °C , which according to Figure B.1 would correspond to approximately 1.2 mTorr. However, measurements taken for adenine required hotter temperatures due to low photon statistics at similar temperatures to thymine. Electron impact measurements were performed at 180 °C as a compromise to obtain similar photon count rates as for thymine, which corresponds to a vapour pressure of 9.2 mTorr. Tabet et al [51] had performed molecular flux measurements on DNA/RNA molecule vapour jets and reported that at 440 K (177 °C), thymine's mass deposit rate was 7 times greater than that of adenine. Whenever the chamber was opened up for maintenance, the mass deposition of adenine from the oven to the top of the chamber where the oven points at was clearly less than that for thymine with the same oven temperature and for similar periods of sublimation.

With these temperatures and vapour pressure estimations, and using $\sigma = 0.7$ nm as an effective diameter for the molecules [51], the mean free path for thymine is estimated to be 16.7 mm at 1.2 mTorr. For adenine, a estimation for the mean free path is 2.34 mm at 9.2

mTorr.

Accordingly, three kinds of flow regime can be described using the Knudsen number K_n, which is related to the dimensions of the capillary (L, the length of the capillary) and the mean free path.

$$K_n = \frac{\lambda}{L} \tag{B.9}$$

Particularly, according to [52], vapour jet flow can be characterized with the following Knudsen numbers

- $K_n > 10$ - molecular flow; no interaction between molecules occurs during exit through capillary
- $K_n > 0.1$ - intermediate flow
- $K_n > 0.001$ - viscous flow; intermolecular collisions are prominent

The length of the biomolecule capillary tube was 20 mm, which suggests an estimated $K_n = 0.83$ for thymine and $K_n = 0.11$, which are both in the intermediate flow range. Thus some collisions will occur between the biomolecules and with the wall of the capillary tube, probably modifying the velocity distribution within the molecular beam exiting the tube.

Appendix C

Detection Efficiency Correction

Measurements made on photon flux across a range of wavelengths was dependent on both the wavelength dependence of the detector and the reflection efficiency of the diffraction grating. To determine accurate relative cross sections, it was necessary to account for this wavelength efficiency by determining an instrument probability function $P(\lambda)$ that suitably reproduces the detection variation. This was done by using a theoretical emission spectrum of H_2 from Brotton et al [6] and as seen in Figure C.1, and comparing it with well-known emission features from an experimentally measured H_2 spectrum. This has been fully discussed in [6].

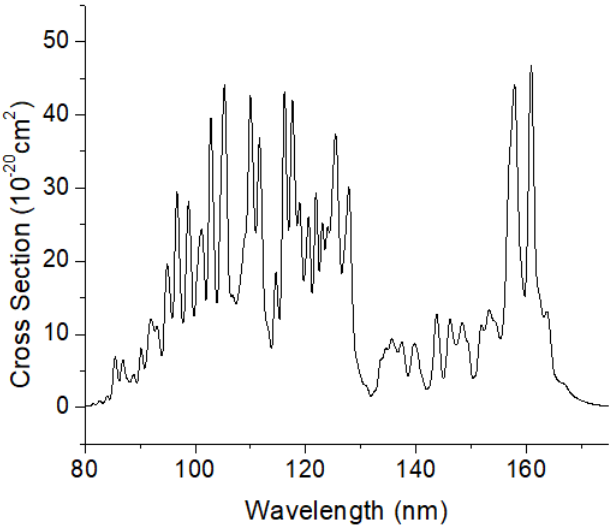

Figure C.1: Theoretical H_2 emission spectrum reproduced from Brotton et al [6].

Firstly, the features of the experimentally measured H_2 spectrum were matched with the features of the theoretical emission spectrum. The ratio between the two sets of data was taken and a cubic polynomial was fitted to the resultant data points. The instrument probability function is shown in Figure C.2. The function begins to rise after 135 nm most likely because the diffraction grating is blazed for maximum reflection at 150 nm.

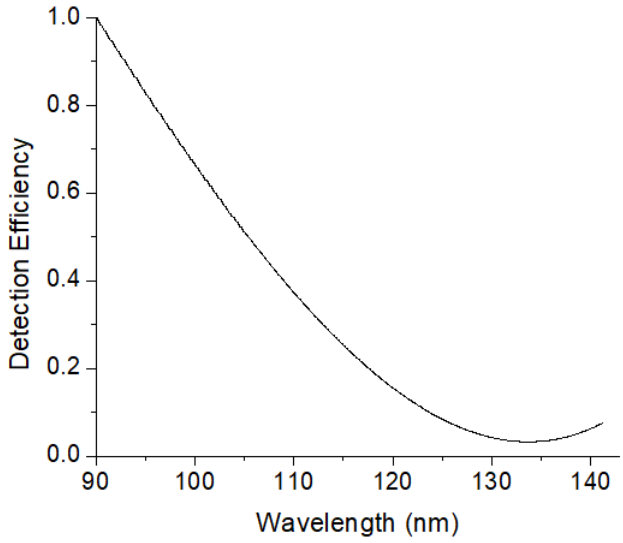

Figure C.2: The relative probability for photon detection from 90 nm to 140 nm. This accounts for the wavelength efficiency for both the detector and diffraction grating.

Appendix D

Threshold Calibration

Helium was a common gas that was used as calibration standard to determine the energy shift in threshold measurements. However, a molecular N_2 signal, appearing at 95.8 nm, was persistent during spectrum measurements. What follows is a calibration calculation that was performed using this background signal. Figure D.1 shows the results of an excitation scan.

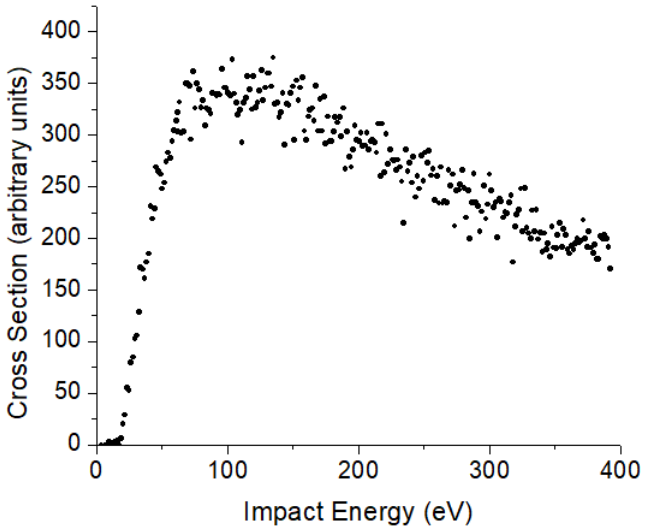

Figure D.1: Excitation study performed on the (0,0) band of the c_4' $^1\Sigma_g^+ \rightarrow ^1\Sigma_g^+$ of N_2 at 95.8 nm.

A linear fit was performed in the near threshold region of the excitation function. The

intercept of this linear fit was calculated as the energy threshold. In this case, it was determined to be 18.2 eV. With a real energy threshold of 12.9 eV for this N_2 feature at 95.8 nm [53], the energy offset was determined to be 5.3 eV.

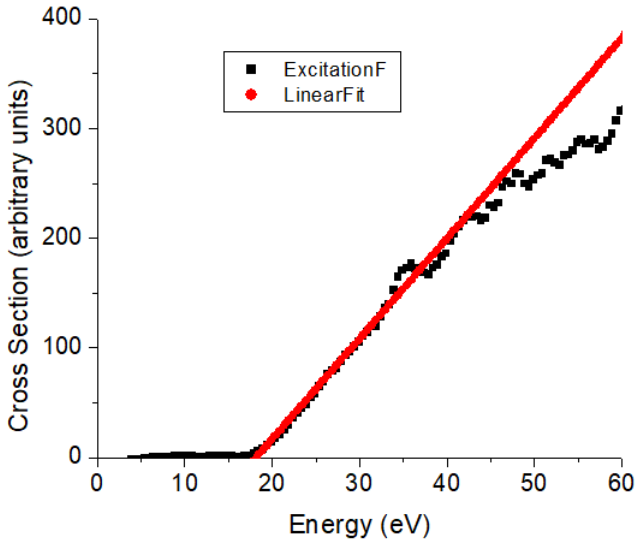

Figure D.2: A close-up of the excitation function measurement along with the linear fit performed near the threshold region.

Appendix E

Curve Fitting and Error Analysis

E.1 Fitting Relative Cross Sections

A Gaussian distribution, f_g, defined as

$$f_g(x) = \frac{A}{\sqrt{\pi w^2/2}} exp\left(-\frac{2(x-x_c)}{w^2}\right) \tag{E.1}$$

with area A, width parameter w, and centre x_c was used to fit the relative cross sections for spectrum scans. The full width at half maximum (FWHM) is expressed as

$$FWHM = 2\sqrt{2\ln 2}w \tag{E.2}$$

E.2 Error Analysis

Standard propagation of errors were used where applicable. Given some quantity f dependent on a set of independent variables $x_1, x_2, ..., x_n$, the uncertainty of f, δf, can be calculated if the corresponding uncertainties for the variables it is dependent on, i.e. $\delta x_1, \delta x_2, ..., \delta x_n$,

are known. The uncertainty is determined by

$$(\delta f)^2 = \sum_{i=1}^{n} \left(\frac{\partial f}{\partial x_i} \delta x_i \right)^2 \tag{E.3}$$

Vita Auctoris

NAME:	Joshuah Anthony Trocchi
PLACE OF BIRTH:	Windsor, ON
YEAR OF BIRTH:	1993
EDUCATION:	University of Windsor, B.Sc., [Honours] Physics, Windsor, ON, 2015
	University of Windsor, M.Sc., Physics, Windsor, ON, 2019